

EXPERIMENTS IN CONTACT CONTROL,

Homayoun Seraji, David Lim, Robert Steele

Jet Propulsion Laboratory, California Institute of Technology
Pasadena, CA 91109

Abstract

This paper describes the implementation, experimentation, and application of contact control schemes for a 7-DOF Robotics Research arm. The contact forces and torques are measured in the sensor frame by the G-axis force/torque sensor mounted at the wrist, are compensated for gravity, and are then transformed to the tool frame in which the contact task is defined and executed. The contact control schemes are implemented on the existing robot position control system at 400 Hz, do not require force rate information, and are extremely simple and computationally fast. Three types of contact control schemes are presented: compliance control, force control, and dual-mode control. In the compliance control scheme, the contact force is fed back through a lag-plus-feedforward compliance controller so that the end-effector behaves like a spring with adjustable stiffness (i.e., a programmable spring); thus the contact force can be controlled by the reference position command. In the force control scheme, a force setpoint is used as the command input and a proportional-plus-integral force controller is employed to ensure that the contact force tracks the force setpoint accurately. In the dual-mode control scheme, the end-effector approaches and impacts the reaction surface in compliance mode, and the control scheme is then switched automatically to force mode after the initial contact has been established. In the compliance mode, this scheme reduces the system sensitivity to the surface location so as to avoid excessive forces at impact. In the force mode, exact contact force regulation is achieved which is robust to the surface stiffness. The paper is concluded with the application of the proposed schemes to perform a contact-based eddy-current inspection task. In this task, the robot first approaches the inspection surface in compliance control until it feels that it has touched the surface, and then automatically levels the end-effector on the surface. The robot control system then transitions to force control and applies the desired force on the surface while executing a scanning motion. At the completion of the inspection task, the robot first relaxes the applied force and then retracts from the surface.

1 Introduction

The need for stable and controlled contact between a robot manipulator and objects in its environment has been the motivation for considerable research in robotics over the past two decades. The outcome of this research has been the development of two categories of contact control schemes: impedance control and force control. In impedance control [1,2], the goal is to establish a desired contact dynamics between the end-effector position and force, rather than to control the contact force directly. On the other hand, the objective of force control [3] is to cause the contact force to follow the commanded force setpoint as closely as possible. The impedance and force control schemes can be implemented either as a torque-based controller which generates the joint torques directly or as a position-based controller which provides a command input for an inner-loop position control system.

This paper describes a set of experiments on contact control carried out on a 7-DOF Robotics Research arm at the NASA-Jet Propulsion Laboratory. Three types of contact controllers are discussed; compliance control, force control, and dual-mode control. The contact control schemes are implemented as position-based controllers using the robot position control system as a baseline. The compliance controller is similar to impedance controller and attempts to establish a desired stiffness between the reference position and the contact force so that the reference position can be used to control the contact force. The force controller accomplishes accurate force setpoint tracking and is robust to variations in the contact surface parameters. The dual-mode control scheme enjoys the combined strengths of both compliance and force control, but does not suffer from their individual weaknesses.

The paper is organized as follows. The real-time manipulator control system used for the experiments is described in Sections 2 and 3. The contact control schemes and their experimental results are discussed in Sections 4 and 5. In Section 6, we present an application of contact control schemes to perform an eddy-current inspection task. The paper is concluded in Section 7 with a discussion of the proposed control schemes.

2 Manipulator Control System

The Jet Propulsion Laboratory is developing an end-to-end robotic system for remote inspection of space structures such as the Space Station Freedom [4]. A basic component of this system is a dexterous robotic manipulator for placement of the inspection sensors. A class of inspection tasks requires physical contact between the sensing element and the inspected surface. In this section, we discuss the basic features of the manipulator control system including hardware, software, and contact control interface.

2.1 Hardware System Description

In this section, we describe the hardware of the manipulator control system. The hardware structure is shown in Figure 1 and consists of a Robotics Research Corporation (RRC) model K 1207 seven degree-of-freedom (DOF) arm/control unit, a VME-based chassis with two MC68040 processor boards and additional interface cards, two hand controllers, a motorized rail/control unit on which the arm is mounted, and a Silicon Graphics IRIS Workstation. Attached to the end of the arm is an integrated sensor/end-effector unit consisting of two CCD cameras with controlled lights, two infrared proximity sensors, a gas sensor, a temperature sensor, a 6-axis force/torque sensor, and a gripper.

The dexterous manipulator used in this study has seven revolute joints in an alternating roll/pitch sequence beginning with the shoulder roll at the base and ending with the tool-plate roll at the hand. The shoulder has both a roll and a pitch DOF, the elbow has an extra roll DOF along the upper-arm in addition to the conventional pitch between the upper-arm and forearm, and the wrist has a roll DOF along the forearm, a pitch between the forearm and hand, and a roll about the tool-plate. The upper-arm roll motion allows the arm plane (formed by the upper-arm and forearm) to rotate about the shoulder-wrist axis, thus providing the capability for arm reconfiguration without perturbing the hand position. The arm pedestal is mounted on a mobile platform of a motorized rail which provides one additional translational degree-of-freedom that can be treated as a prismatic joint. Therefore, the complete manipulator system has eight independent joint, degrees-of-freedom. This system has two degrees-of-redundancy, i.e. two 'extra' joints, since six joints are sufficient for the basic task of end-effector position and orientation control in the three-dimensional workspace. In the experiments described here the motorized platform is fixed during task execution, thus the system is treated as a 7-DOF robot.

The RRC arm is controlled by a real-time microprocessor-based controller that uses advanced ccd control algorithms for high-level dexterous motion control and interfaces directly with the Multibus-based arm control unit supplied by the manufacturer. The real-time controller is a VMEbus-based system that uses two Motorola MC68040 processors along with various data acquisition, memory, and communication devices. The VME controller is linked via socket communication to a Silicon Graphics IRIS Workstation, which serves as the host computer for the graphical user interface. The control structure simplifies the integration of future generations of higher-performance hardware and new control techniques as they become available, and thus provides a growth capability that extends the technical life of the arm control system.

A high-speed bus interface is used to communicate between the real-time VME chassis and the arm control unit Multibus chassis. This enables communication with the arm control unit at high speed (400 Hz) via a shared memory servo level interface. The reason for this

design choice is to have 110 software development 011 the Multibus system. Thus, the control system 011 the VME chassis treats the arm control unit as a joint-space position controller.

2.2 Control System Description

The manipulator Cartesian control flow diagram is shown in Figure 2. The configuration control technique [5-8] developed at JPL, is implemented in the VME environment for the 7-DOF RRC arm. The major algorithms for the control system are the: forward kinematics and Jacobian computations, a singularity-robust configuration control computation, real-time trajectory generation routines, and contact control algorithms. The various algorithms will be discussed in this section with the exception of the contact control algorithms which will be addressed in Section 4. The interface to the contact control algorithms will be discussed in this section.

2.2.1 Kinematics Computations

The computations of the forward kinematics and Jacobian of the manipulator utilize Craig's interpretation of Denavit-Hartenberg (DH) parameters for frame assignment [9,10]. This method provides direct computation of the manipulator Jacobian J in the world frame of the robot. The configuration control approach is implemented for resolution of redundancy and computation of inverse kinematics. This approach allows the user to define additional tasks with assigned weights for redundancy resolution, and yields the singularity-robust inverse kinematic computation:

$$\dot{\theta}_d = [J^T W_t J + W_v]^{-1} J^T W_t [\dot{X}_d + K E] \quad (1)$$

where W_t and W_v are the task-space error weights and joint velocity damping weights, $E = X_d - X$ and K is a diagonal matrix with positive elements. Note that (1) can also be written as:

$$\dot{\theta}_d = [J_e^T W_e J_e + J_c^T W_c J_c + W_v]^{-1} [J_e^T W_e \dot{Y}_d + K_e E_e + J_c^T W_c \dot{Z}_d + K_c E_c] \quad (2)$$

where the subscript e refers to the basic task $Y = Y_d$ of positioning the hand, and the subscript c refers to additional tasks $Z = Z_d$ for redundancy resolution. Cholesky decomposition is used to solve (2). Equation (1) relies on weighting joint velocities against task-space position errors. It can be seen that as the Jacobian becomes singular, the velocity weight dominates in the inverse matrix term in (1), reducing the commanded joint velocities. The reduced joint velocities, in turn, act to retard the arm from reaching the singular configuration.

In the present implementation, arm angle control is chosen as the seventh task. The “arm angle” is defined as the angle between the arm plane SFW and the vertical plane passing through the line SW, where S, E and W refer to the origins of the shoulder, elbow and wrist frames, respectively. This angle uniquely specifies the elbow position for a given hand frame, and together with the hand coordinates gives a complete representation of the geometric posture of the whole arm in almost the entire workspace. In the control software, we use a simple and efficient method described in [10] for computing the arm angle and the associated constraint Jacobian.

In addition to the seven basic tasks, an additional task is defined for each joint that is near its limit using the configuration control framework. When joint limits are approached, the system actually becomes “deficient” (as opposed to being “redundant”). The configuration control algorithm automatically relaxes certain tasks based on their weightings. The joint limit avoidance task is formulated as an inequality constraint that is activated only when the joint is within its “soft” limit, and is inactive otherwise. Interestingly, the formulation of the extra tasks is extremely simple. Observe that $J_\zeta^T W_\zeta J_\zeta = W_\zeta$ and that $J_\zeta^T W_\zeta$ reduces to W_ζ , where ζ indicates the joint limit avoidance task. Thus computationally the joint limit avoidance task is extremely fast. To avoid chattering when the joint limit avoidance task is activated and deactivated, W_ζ is formulated as a continuous function of θ , e.g. at the lower joint limit:

$$W_\zeta = \begin{cases} 0 & \theta \geq \theta_{soft} \\ \frac{W_{max}}{2} \left[1 - \cos \pi \left(\frac{\theta - \theta_{soft}}{\theta_{hard} - \theta_{soft}} \right) \right] & \theta_{hard} < \theta < \theta_{soft} \\ W_{max} & 0 \leq \theta < \theta_{hard} \end{cases} \quad (3)$$

where θ_{soft} and θ_{hard} are the soft and hard joint limits.

2.2.2 Trajectory Generation

Two different trajectory generators are implemented in the system. The first trajectory generator produces smooth continuous cycloidal functions to make a straight-line transition from the initial to the final values in the specified time [5]. A second via-point blending trajectory generator is also implemented in the system [11]. The via-point blending trajectory generator allows the specification of several via-points. The algorithm generates a smooth trajectory between the points, while gradually blending the velocities from one via-point to the next.

2.2.3 Contact Control interface

In this section, we discuss two issues related to implementation of contact control schemes: namely, coordinate transformation and trajectory perturbation.

Coordinate Transformation: A basic issue in contact control is the selection of the appropriate frame of reference. Two choices are commonly available: the stationary world frame $\{W\}$ fixed in the workspace, and the moving tool frame $\{T\}$ attached to the tip of the tool grasped by the end-effector. The force/torque sensor is mounted at the end-effector such that the sensor frame $\{S\}$ is rotationally aligned with the end-effector frame; otherwise an additional transformation is needed. The tool frame is often obtained by translating the end-effector frame along the end-effector z-axis by the tool length. For contact tasks, it is more convenient to describe the task to be performed in the tool frame $\{T\}$. Typically, the end-effector approaches and contacts the reaction surface along the z-axis of $\{T\}$. Therefore, in our study, the tool frame $\{T\}$ is chosen as the contact frame of reference. As a consequence, the parameters of the contact controller are also specified in the tool frame. Now, since the reference position trajectory is specified in the world frame $\{W\}$, the position perturbation X_f generated by the contact controller must be transformed from $\{T\}$ to $\{W\}$ to modify X_r . This transformation is given by

$${}^w X_f = \begin{pmatrix} {}^w \Delta p \\ {}^w \Delta \phi \end{pmatrix} = \begin{pmatrix} {}^w R^t \Delta p \\ {}^w R^t \Delta \phi \end{pmatrix} \quad (4)$$

which only involves the rotation matrix ${}^w R^t$ from $\{T\}$ to $\{W\}$, [9,p.58]. In (4), Δp and $\Delta \phi$ denote the positional and orientational perturbations and the leading subscript is the frame of reference. Notice that the elements of A^+ produced by the contact controller are treated as independent orientation perturbations about the coordinate axes, i.e. as changes in the equivalent angle-axis representation of orientation.

Trajectory Perturbation: We shall now examine closely the trajectory perturbation caused by the contact controller. As shown in Figure 3, the contact control scheme is implemented as the outer feedback loop to generate the position perturbation X_f which modifies the reference position X_r to produce the position setpoint X_d which is sent to the arm control system for tracking. Let the current position and orientation of the tool relative to $\{W\}$ be given by the 4x4 transformation matrix

$$T_1 = \begin{pmatrix} R_1 & p_1 \\ 0 & 1 \end{pmatrix} \quad (5)$$

where R_1 is the 3x3 rotation matrix which describes the end-effector orientation, and p_1 is

the 3x1 position vector denoting the end-effector position. Let the 6x1 vector X_f generated by the contact controller be defined as

$$X_f = \begin{pmatrix} \Delta p \\ \Delta \phi \end{pmatrix} \quad (6)$$

where Δp represents the three translational (i.e. position) perturbations, and $\Delta \phi$ denotes the three rotational (i.e. orientation) perturbations around each axis. Then, for the translational elements, we simply have

$$p_2 = p_1 + \Delta p \quad (7)$$

For the rotational perturbations, we first compute the 3x3 rotational matrix AR from $\Delta \phi$ which describes the relative change in orientation [9,p.52]. Then, the current end-effector rotation matrix R_1 is modified to

$$R_2 = R_1 \cdot AR \quad (8)$$

where the rotation matrices are treated as operators. Thus, the modified position and orientation of the end-effector are given by

$$T_2 = \begin{pmatrix} R_2 & p_2 \\ 0 & 1 \end{pmatrix} \quad (9)$$

This matrix provides the setpoint X_d for the inner Cartesian position control system of the arm for tracking.

2.3 Software Architecture

In this section, we discuss the software components of the VME environment used for real-time control of the manipulator. All of the software executing in the VME environment is written in the C language. The code is developed on a SUN UNIX Workstation utilizing the Wind River's development environment and the vxWorks real-time kernel as the operating system. This environment consists of a C compiler, a remote symbolic debugger, and the Stethoscope real-time monitoring software tool. The code is downloaded through Ethernet to the target processor boards for execution.

Figure 4 shows the software structure of the VME-based controller. The VME chassis hosts two Motorola MV167 MC68040 CPU cards that perform all the necessary computations to provide real-time control of the manipulator. The user *interface(ui) task* interfaces with the high-level system residing in the IRIS to receive user commands and to send acknowledgment and state information after execution of the commands. The information is routed bi-directionally through Ethernet using UNIX sockets. Once a command is received from the IRIS, the *ui task* parses the command and then writes appropriate command information into the shared memory card to pass the data along to the other tasks. All commands from the IRIS are acknowledged by the controller. Every reply from the controller contains the state of the system which includes information such as sensor data, current joint angles, current mode, and Cartesian task values.

The *hand controller task* is designated to perform data acquisition. It controls the activities of the Analog-to-Digital (A/D) converter boards which are used to read in baud controller inputs and sensor data. The first A/D board reads in various voltage outputs of the six potentiometers on the hand controllers. In addition, it monitors the three switches on the rotational grip hand controller. The second A/D board reads in the sensor data from the temperature sensor, gas sensor, and the two proximity sensors. The *hc task* currently runs at 33 Hz.

The *force/torque sensor(fls) task* reads the force/torque sensor data through the A/D board at 400 Hz, and deposits the data into shared memory.

The *control(ctrl) task* performs real-time trajectory generation, kinematic computations, and contact control. Both automated and teleoperated moves are supported in all three modes: joint mode, Cartesian world mode, and Cartesian tool mode. In Cartesian mode, the arm can be moved with reference to its tool frame (tool mode) or an absolute base frame (*world* mode). *Tool* mode enables the user to move the joints of the robot in a coordinated manner such that the user has the notion of moving the tool as if it is being held by the user's hand (e.g., holding onto a screwdriver and moving the handle to control the tip of the screwdriver). *World* mode is used when the user wishes to move the robot with respect to a fixed user-defined frame. The trajectory generation, kinematics and Jacobian computations, configuration centroid computation, Cholesky decomposition, and centroid control computation take approximately 2 ms to complete. In this process, the differential desired Cartesian commands (ΔX_d) are converted to differential desired joint commands ($\Delta \theta_d$), which are then integrated and the desired joint angles θ_d are sent to the arm control unit for execution.

The **Robotics Research servo(rrs) task** is designated to execute the arm interface driver at every servo cycle, thereby maintaining constant communication with the arm control unit. The arm control unit has the **Electronic Servo-1 level Interface**, which allows the user to communicate directly with the joint servo motors through dual-port memory locations on the RRC system. The maximum rate of communication is 400 Hz (i.e., a sampling period of

2.5ms). Each joint servo motor can be independently commanded in any of the four modes: position, velocity, torque, and current. This feature enables the operation of the robot under both kinematic and dynamic control schemes, and therefore facilitates validation of a variety of arm control laws. The feedback information such as the actual position, velocity, and torque values are also accessible from the dual-port memory. We are presently communicating at the maximum rate of 400 Hz, and all seven joints are commanded in position mode. The driver performs all the necessary handshakes with the arm control unit software and conversion of data into appropriate formats. In addition, joint position and velocity limits are also checked at each cycle for safety reasons.

3 Gravity Compensation

To properly measure the forces and torques exerted by the manipulator on the environment, the weight of the tool beyond the Force/Torque ($1\frac{1}{2}$ lb) sensor must be compensated for. This section describes the gravity compensation calculations used in the control system.

The payload extending beyond the F/T sensor is modeled as a point mass with a center of gravity at a distance d beyond the F/T sensor frame, as shown in Figure 5. Note that the world frame is defined with the z-axis aligned with gravity but in the opposite direction. Without loss of generality, the F/T sensor frame is assumed to be aligned with the tool frame. If the physical sensor is not aligned with the tool frame, an additional transformation can be applied to obtain the measured forces and torques in the sensor frame as defined here.

The following notational conventions are used:

- a leading superscript indicates the frame of reference
- a leading subscript indicates the frame of reference of interest relative to the specified frame of reference
- a superscript indicates a name
- a subscript indicates a point in space
- F - force
- N - torque
- R - rotational matrix

Thus

$${}^w J_g^{grav}$$

indicates the force due to gravity exerted at point g expressed in the $\{W\}$ frame. Similarly

$${}^s R$$

is the rotation matrix expressing the $\{W\}$ frame in the $\{S\}$ frame. The relevant frames are the world frame $\{W\}$, the F/T sensor frame $\{S\}$, and the frame $\{G\}$ at the center of gravity of the tool in the end-effector. The frame $\{G\}$ is also chosen to be rotationally aligned with the $\{S\}$ frame. The distance d is measured along the positive z-axis of the sensor frame. Let us assume for now that the values for d and the weight of the tool, E , are known. Thus

$${}^w J_g^{grav} = (0, 0, E)^T$$

For gravity compensation, we need to determine the effect of the tool weight on the sensor:

$${}^s J_g^{grav} \text{ and } {}^s N_g^{grav}$$

i.e., the forces and torques exerted on the sensor due to the tool weight, in the sensor frame $\{S\}$. The values of these forces and torques can then be subtracted from the measured forces and torques by the sensor to determine the true forces and torques exerted by the environment on the sensor. These forces and torques can then be used in the contact control algorithms. The usual convention is to consider the forces and torques exerted on the environment by the manipulator, which simply involves changing the sign of the gravity compensated forces and torques reported by the F/T sensor. The contact control algorithms can also apply a transformation to these forces and torques to determine the forces and torques at the point of contact, or at the point of interest in the environment. Note that the amount of gravity compensation changes with the configuration of the arm. The force-torque transformation on a rigid body is given by [9,p.181]:

$$\begin{pmatrix} {}^s J_g^{grav} \\ {}^s N_g^{grav} \end{pmatrix} = \begin{pmatrix} {}^s R & 0 \\ {}^s P_g \times {}^s R & {}^s R \end{pmatrix} \begin{pmatrix} {}^g J_g^{grav} \\ {}^g N_g^{grav} \end{pmatrix} \quad (10)$$

Since we assumed that the $\{G\}$ frame is rotationally aligned with the $\{S\}$ frame, sR is the identity matrix. Evaluating the terms on the right-hand-side of (10),

$${}^sP_g \text{ is the vector } \begin{pmatrix} 0 \\ 0 \\ d \end{pmatrix}$$

$${}^sP_g \times \text{operator is thus } \begin{pmatrix} 0 & -dd & 0 \\ d & 0 & 0 \\ 0 & 0 & 0 \end{pmatrix}$$

The second term on the right-hand-side of (10) can be calculated as follows:

$${}^gF_g^{grav} = {}^gR {}^sF_g^{grav} = {}^sF_g^{grav} = {}^wR {}^wF_g^{grav} = {}^wR \begin{pmatrix} 0 \\ 0 \\ E \end{pmatrix} = \begin{pmatrix} a_0 \\ a_1 \\ a_2 \end{pmatrix} E$$

where $(a_0, a_1, a_2)^T$ is the third column of wR , and is known from forward kinematics of the manipulator. Similarly,

$${}^gN_g^{grav} = {}^sP_g \times {}^gF_g^{grav} + {}^gR {}^sN_g^{grav}, \quad {}^sN_g^{grav} = {}^wR {}^wN_g^{grav} = 0$$

since sP_g and ${}^wN_g^{grav}$ are zero. The tool does not generate any torques in free motion. Thus (10) reduces to:

$${}^gF_g^{grav} = {}^gF_g^{grav} = \begin{pmatrix} a_0 \\ a_1 \\ a_2 \end{pmatrix} E \quad (11)$$

$${}^sN_g^{grav} = \begin{pmatrix} -a_1 \\ a_0 \\ 0 \end{pmatrix} dE \quad (12)$$

Equations (11) and (12) are the gravity compensation values. They can be subtracted directly from the measured forces and torques of the sensor expressed in the sensor frame $\{S\}$. Thus

$${}^sF_s^{comp} = {}^sF_s^{meas} - {}^sF_g^{grav} \quad (13)$$

$${}^s N_s^{comp} = {}^s N_s^{meas} - {}^s N_s^{grav} \quad (14)$$

Once the true contact forces and torques are found in {S}, the gravity-compensated contact forces and torques in the tool frame {T} are obtained as [9,p.181]:

$$\begin{pmatrix} {}^t F_t^{comp} \\ {}^t N_t^{comp} \end{pmatrix} = \begin{pmatrix} {}^t R & 0 \\ {}^t P_s \times {}^t R & {}^t R \end{pmatrix} \begin{pmatrix} {}^s F_s^{comp} \\ {}^s N_s^{comp} \end{pmatrix} \quad (15)$$

where ${}^t R$ is the identity matrix, since the frames {S} and {T} are rotationally aligned, and ${}^t P_s = (0, 0, -l)^T$ where l is the distance between the origins of {S} and {T}. Note that using equations (11) and (12), the weight of the tool, F , and the distance to the center of gravity, d , can be determined experimentally with the F/T sensor and the manipulator. This is done by placing the sensor frame in a known configuration without being in contact with the environment. In this case, the compensated forces and torques by definition are zero. It is simplest to align the tool frame with the principal axes of the world frame. If the tool frame is placed such that it is aligned with the world frame z-axis, then $a_0 = a_1 = 0$, and $a_2 = 1$. Then the measured force by the sensor should be equal to the weight of the tool, i.e.

$${}^s F_s^{meas} = \begin{pmatrix} 0 \\ 0 \\ F \end{pmatrix}$$

Once F is determined, the sensor frame z-axis can be aligned with the world z-axis. In this case, $a_0 = 1$, $a_1 = a_2 = 0$, and d can be calculated from (12) and (14) as:

$${}^s N_s^{meas} = \begin{pmatrix} 0 \\ dF \\ 0 \end{pmatrix}$$

Note that there are an infinite number of poses that can be used for determination of F and d . In practice, we have used the two permutations of aligning with the world z-axis to get the average weight of the tool, and the four permutations of aligning with the world x and y axes to obtain an average value for d .

Determining the value of F and d with this method has its disadvantages. The accuracy of the values is dependent on the accuracy of the forward kinematics and the joint positional accuracy of the manipulator. It is probably better to determine F and d by other methods, and use the above method to check the kinematic accuracy of the manipulator.

4 Contact Control Schemes

In this section, we discuss three types of contact control schemes; namely, compliance control, force control, and dual-mode control. The contact control schemes operate in the user-defined tool frame $\{7\}$ where the task is defined and executed. The dynamic modeling and stability analysis of the proposed position-based contact control systems are studied in [13]. In this section, the results are presented without proof. Note that the term “position” implies position or orientation, and the term “force” implies force or torque.

4.1 Compliance Control

A manipulator under Cartesian position control in contact with a reaction surface can be adequately described in each Cartesian direction of contact by the second-order transfer function [13]

$$\frac{F(s)}{X_r(s)} = \frac{ck_e}{s^2 + as + b} \quad (16)$$

where k_e is the surface stiffness, $[a, b, c]$ are the manipulator constants, and the origin of the frame-of-reference is the point of contact between the end-effector and the reaction surface with the x-axis in the direction of the applied force. There are four major sources of compliance in the system due to: (i) the reaction surface where contact is made, (ii) the force/torque sensor that measures the end-effector/surface interaction, (iii) the joint servo loops of the manipulator which have finite stiffness, and (iv) the joint gear transmission system. From (16), the steady-state contact force F is related to the position command X_r by

$$F = \frac{ck_e}{b} \cdot X_r = k_f \cdot X_r \quad (17)$$

It is seen that the environment “appears” as a spring with the stiffness coefficient $k_f = ck_e/b$ to the position command, where k_f is typically a large number. The basic concept of the compliance control system shown in Figure 6 is to use force feedback in order to reduce the forward gain or stiffness k_f in the end-effector/reaction surface interaction. This will then allow the reference position X_r to be used as a command input to control the contact force F as the output. Under compliance control, the reference trajectory is used differently for the two categories of tasks: as the desired motion trajectory in unconstrained tasks and as the input command to control the contact force in constrained tasks. This is in contrast to force control schemes in which a force setpoint is used to command the contact force.

The compliance controller used in this paper consists of the first-order lag $k_1/(\tau s + 1)$ in parallel with the feedforward gain k_2 as shown in Figure 6, where $[k_1, k_2, \tau]$ are constant parameters of the controller. This yields the compensator transfer-function

$$K(s) = \frac{k_1}{\tau s + 1} + k_2 = \frac{\alpha s + \beta}{\tau s + 1} \quad (18)$$

where $\alpha = \tau k_2$ and $\beta = k_1 + k_2$. Notice that $K(s)$ can be expressed as the “proportional-plus-filtered-derivative” controller $K(s) = k_p + \frac{1}{\tau s + 1} k_d s$, where $k_p = \beta$ and $k_d = \alpha - \beta\tau$. Hence the low-pass filter $\frac{1}{\tau s + 1}$ removes the high-frequency noise superimposed on the measured contact force *before* differentiation.

Applying the compliance controller $K(s)$ given by (18) to the open-loop system (16) yields the closed-loop transfer-function

$$\frac{F(s)}{X_r(s)} = \frac{ck_e \tau s + ck_e}{\tau s^3 + [a\tau + 1]s^2 + [a + b\tau + ck_e \alpha]s + [b + ck_e \beta]} \quad (19)$$

It can readily be shown that since $[a, b, c, k_e, \tau]$ are positive, for closed-loop stability we require

$$\alpha_{min} < \alpha \quad ; \quad \beta_{min} < \beta < \beta_{max} \quad (20)$$

where

$$\alpha_{min} = \frac{a + b\tau}{ck_e} \quad ; \quad \beta_{min} = \frac{b}{ck_e} \quad ; \quad \beta_{max} = \frac{a + a^2\tau + ab\tau^2}{ck_e\tau} + \alpha \left[a + \frac{1}{\tau} \right] \quad (21)$$

Therefore, to ensure stability, it is *sufficient* to have

$$0 < \beta < \alpha \left[a + \frac{1}{\tau} \right] \quad (22)$$

A more conservative *sufficient* condition for closed-loop stability is found to be

$$0 < \frac{\beta}{\alpha} < \frac{1}{\tau} \quad (23)$$

which ensures that $K(s)$ is a phase-lead compensator. Now, the steady-state relationship between the reference position X_r and the contact force F is obtained from (19) as

$$F = \frac{ck_e}{b + ck_e\beta} X_r = \frac{1}{k_f^{-1} + \frac{1}{\beta}} X_r = k_{ap} X_r \quad (24)$$

It is seen that under compliance control, the reaction surface “appears” as a spring with the, apparent stiffness $k_{ap} = [k_f^{-1} + \beta]^{-1}$. This is the equivalent stiffness of the series combination of the two springs k_f and β^{-1} representing the stiffnesses of the open-loop system and the compliance controller, respectively. From (24), we conclude that given the open-loop stiffness k_f , the controller stiffness β can be chosen such that the closed-loop system exhibits the desired stiffness, provided that the stability conditions (20) are not violated. observe that increasing β will reduce k_{ap} and make the end-effector more compliant to applied forces, since $k_{ap} = [1 + \beta k_f]^{-1} k_f$ reveals that the open-loop stiffness k_f is altered by the factor $[1 + \beta k_f]^{-1}$ to produce the closed-loop stiffness k_{ap} . Note that for hard contacts, $k_{ap} \approx 0$. Equation (24) provides a practical means to control the contact force F by the position command X_r . Notice that the compliance controller (18) does *not* require the force derivative \dot{F} for implementation.

4.2 Force Control

In contrast to compliance control which is an implicit force control scheme, in this section we describe an *explicit* force control scheme. in explicit force control, or force control for short, the force setpoint F_r is used as the command input to control the contact force F directly as shown in the block diagram of Figure 7, and the position command X_r is deactivated (held constant) during the execution of the contact task. The force controller $K(s)$ now uses the force error information $e = F - F_r$ to generate the necessary control action so that the contact force F tracks the force setpoint F_r .

The force controller used in this paper is the proportional-plus-integral (PI) controller

$$K(s) = k_p + \frac{k_i}{s} \quad (25)$$

where k_p and k_i are the constant proportional and integral force feedback gains respectively. This yields the force feedback law

$$X_f(t) = k_p e(t) + k_i \int_0^t e(t) dt \quad (26)$$

where X_f is the position perturbation produced by the force controller. Applying the force controller $K(s)$ given by (25) to the open-loop system (16) yields the closed-loop transfer-function

$$\frac{F(s)}{F_r(s)} = \frac{ck_e k_p s + ck_e k_i}{s^3 + as^2 + [b + ck_e k_p]s + ck_e k_i} \quad (27)$$

Since $[a, b, c, k_e]$ are positive, it can be shown that for closed-loop stability we require

$$0 < k_i < a[k_p + k_f^{-1}] \quad (28)$$

Therefore, to ensure stability, it is *sufficient* to have

$$0 < k_i < ak_p \quad (29)$$

which is independent of the reaction surface stiffness k_e . Now, assuming closed-loop stability, the steady-state response of the contact force F to the constant force setpoint F_r is obtained from (27) as

$$F = \lim_{s \rightarrow 0} sF(s) = F_r \quad (30)$$

Thus, the contact force tracks the force setpoint accurately with zero steady-state error. In fact, it can readily be shown that the closed-loop system rejects any step disturbances due to the position command X_r or a force disturbance F_d in the sense that the contact force F will exhibit a transient response but will not be affected in the steady-state. Furthermore, the system is robust to parameter variations so that the steady-state setpoint tracking and disturbance rejection characteristics are preserved, provided that the closed-loop system remains stable. These inherent features of the integral term make it a vital component in any practical explicit force control scheme.

4.3 Dual-Mode Control

In this section, we introduce a dual-mode contact controller for robotic manipulators. The controller is represented by the transfer-function

$$K(s) = \frac{\alpha s + \beta}{\tau s + 1} \quad (31)$$

where $[\alpha, \beta, \gamma, \lambda]$ are constants. This controller is used in two modes of operation: compliance control or force control. For the compliance control mode, we set $\lambda = 1$ and $\tau = \tau$ (a user-specified small positive number) so that $K(s) = \frac{1}{\tau s + 1} \cdot [\alpha s + \beta]$ acts as a 'filtered-PI' compliance controller discussed in Section 4.1. In this mode, the controller input is the contact force F and the output is the position perturbation X_j . This controller reduces the

Mode Parameter	Compliance	Force
γ	1	1
λ	1	0
α	k_d	k_p
β	k_p	k_i
controller input	F	$F - F_r$
command input	X_r	F_r

Table 1: Dual-mode controller parameters

apparent stiffness of the reaction surface, and thus avoids the generation of excessive force at impact compared to pure position control [$K(s) = 0$]. For the force control mode, we set $\gamma = 1$ and $\lambda = 0$ so that $K(s) = \alpha + \frac{1}{s}\beta$ acts as a PI force controller discussed in Section 4.2. This controller is driven by the force error $e = F - F_r$, where F and F_r are the actual and desired contact forces, and produces the position perturbation X_f . This controller ensures that the contact force F tracks the force setpoint F_r accurately and rejects disturbances due to X_r in the steady-state. The switching between the two modes is based on the value of the measured contact force F . When $|F| < F_T$, where F_T is a user-specified positive threshold level, we operate in the compliance control mode. When $|F| \geq F_T$, we switch mode automatically and operate in the force control mode.

In summary, compliance control is used during the end-effector approach and impact phase. This takes care of the uncertainty in the reaction surface location, and significantly reduces the impact force compared to pure position control, since the end-effector behaves like a soft spring. After the initial contact is established, the controller switches automatically to force control mode to apply the desired contact force during the execution of the contact task. This takes care of the uncertainty in the reaction surface stiffness for achieving exact force control. We conclude that the dual-mode control scheme takes advantage of both compliance and force control schemes during the operation. Observe that this scheme can be viewed as using "gain-scheduling" for the contact controller (31). Table 1 summarizes the parameter values for each mode of operation. Note that pure position control can be retrieved by setting $e = 0$.

5 Experimental Results

In this section, we present a set of experimental results on contact control using the three contact controllers discussed in Section 4. The robotic manipulator used in these experiments is the 7-DOF Robotics Research Corp. (RRC) arm described in Section 2, and carries a model 15/50 6-DOF Assurance Technologies force/torque sensor mounted at the wrist. The configuration control approach developed at JPL [8] is implemented as the baseline arm position control system. In unconstrained free-space motion tasks, this control system ensures that the end-effector position and orientation, as well as a seventh user-specified task variable such as the arm angle, track user-defined desired task trajectories accurately,

During contact with a reaction surface, the force/torque sensor measures the contact forces and torques. This sensory data is then fed back to the real-time arm control system where it is ‘corrected’ by the gravity compensation software module described in Section 3 to obtain the 6x1 vector F of the true contact forces and torques. Each element of F is then passed through a contact controller which produces the position perturbation X_c to the reference motion trajectory X_r . The real-time system runs at the sampling frequency of 400 Hz. Since the tool contacts the surface in only one direction, the z-axis of the tool frame is considered for contact control and the x and y translational motions as well as the three rotational motions of the end-effector are operated under pure position control. Note that in the contact experiments, the x and y axes of the tool frame $\{T\}$ are parallel to and in the same direction as the x and y axes of the world frame $\{W\}$, while the z axes of the two frames are parallel but in opposite directions. The force setpoints and contact forces discussed in this section are expressed in the world frame and should be changed in sign for the tool frame. In this experimental study, two types of reaction surfaces are considered: a ‘soft’ surface which is a cardboard box and a ‘hard’ surface which is a steel plate. *No passive damping elements, such as rubber padding or sponge, are used to reduce the end-effector stiffness.*

Four sets of experiments are now described:

5.1 Experiment 1: Open-Loop Response

Before describing the contact control experiments, a simple test is conducted *without* force feedback by setting $K(s) = 0$ and operating under pure position control. The end-effector is commanded with the hand controller to move down and ‘make contact with the steel plate resting on a table’. The end-effector position coordinate and contact force are recorded during the experiment and are depicted in Figures 8a-8b. From these figures, it is seen that a change in position of $\Delta z_r = 3.32$ mm produces a change in contact force of $\Delta F = 42.86$ N. Therefore, in the absence of force feedback, the stiffness of the manipulator is equal to

$$k_f = \frac{\Delta F}{\Delta z_r} = 12.91 \text{ Nt/mm} \quad (32)$$

This is largely due to the compliance of the joint servo loops and gear trains since the reaction surface and force/torque sensor are both very stiff.

5.2 Experiment 2: Compliance Control

Experiment 1 is repeated but this time the contact force is fed back through a compliance controller to reduce the end-effector stiffness, as discussed in Section 4.1. The compliance controller used is

$$K(s) = 10^{-3} \frac{0.01s + 0.5}{0.05s + 1} = 10^{-3} \frac{\alpha s + \beta}{\tau s + 1} \quad (33)$$

where 10^{-3} converts the unit of the controller output from millimeter to meter. The lag time-constant $\tau = 0.05$ is chosen so that the cutoff frequency of the low-pass filter is at 20 rad/sec. The controller gains $\alpha = 0.01$ and $\beta = 0.5$ were found empirically. Under compliance control, the end-effector is commanded to approach and make contact with the steel plate resting on the table. Figures 9a-9b show the variations of the end-effector position z_r and the filtered contact force F during the experiment. From these figures, it is seen that a position change of $\Delta z_r = 10$ mm produces a force change of $\Delta F = 17.5$ Nt. Therefore, the apparent stiffness of the steel plate as seen by the position command z_r is

$$k_{ap} = \frac{\Delta F}{\Delta z_r} = 1.75 \text{ Nt/mm} \quad (34)$$

in comparison with experiment 1, it is evident that the compliance controller has caused a reduction in the stiffness from 12.91 to 1.75, which is a change by a factor of 7.4. The position command z_r can now be used to control the contact force F through the relationship

$$\Delta F = k_{ap} \cdot \Delta z_r \quad (35)$$

Observe that Figure 9b also shows the perturbed motion trajectory $z_d = z_r - z_f$ which is tracked by the robot position control system.

The experiment is now repeated using the cardboard box as the reaction surface but with the same compliance controller $K(s)$ as before. The plots of the commanded position z_r and the filtered contact force F are depicted in Figures 9c-9d. It is seen that the same position

change of 10mm now causes a smaller force change of 12.86Nt; hence the apparent stiffness of the box is

$$k_{ap} = 1.286 \text{ Nt/mm} \quad (36)$$

Notice that the equivalent stiffness during soft contact is smaller than that during hard contact, as expected. Furthermore, k is always smaller than both the surface stiffness and the controller stiffness (β^{-1}), assuming $\beta > 0$.

5.3 Experiment 3: Force Control

in this experiment, the end-effector is operated under force control and makes contact with both the hard surface (steel plate) and the soft surface (cardboard box). The force controller used is

$$K(s) = 10^{-3} \left[0.05 + \frac{1.5}{s} \right] = 10^{-3} \left[k_p + \frac{1}{s} k_i \right] \quad (37)$$

which is of proportional-integral type as discussed in Section 4.2. The values $k_p = 0.05$ and $k_i = 1.5$ were found experimentally, and 10^{-3} converts the controller output from millimeter to meter. The system is driven by the force setpoint of $F_r = -10 \text{ Nt}$ initially, and subsequently the setpoint is changed to -20 Nt and 0 Nt . The experimental data is depicted in Figure 10a and shows that the contact force F tracks the force command F_r very accurately in all three cases of $F_r = -10, -20, 0 \text{ Nt}$. The transient response shows slight oscillations which are damped out very rapidly. To demonstrate the disturbance rejection property of the force control system, the experiment is repeated with $F_r = -10 \text{ Nt}$. After the contact force reaches the steady-state value of $F = F_r = -10 \text{ Nt}$, the position input z_r is perturbed by 10mm away from the surface followed by 10mm toward the surface, Figure 10b shows the response of the contact force F to this disturbance input. It is seen that the contact force F is decreased momentarily due to the decrease in z_r , and is then restored rapidly to the force setpoint $F_r = -10$; and subsequently F is increased momentarily due to the increase in z_r , but is restored rapidly to F_r . Thus the disturbance input z_r has no steady-state effect on the contact force F . From Figures 10a- 10b, we conclude that the force control system has demonstrated the properties of command tracking and disturbance rejection.

The experiment is now repeated with the soft surface (cardboard box) using the same force controller $K(s)$ as before. Using a staircase force setpoint of $F_r = -10, -20, 0 \text{ Nt}$, the response of the contact force F is shown in Figure 10c. It is evident that the contact force tracks the force setpoint very closely for all cases with no overshoot and a fast transient response. In comparison with Figure 10a, it is seen that using the same force controller $K(s)$ the force response has damped oscillations with a large peak overshoot for hard surface contact but exhibits a non-oscillatory response for soft surface contact. This is expected in view of the fact that the high surface stiffness yields a large loop gain which makes the system oscillatory, whereas the low surface stiffness produces a small loop gain, thus preventing oscillations.

5.4 Experiment 4: Dual-Mode Control

As seen in experiment 2, compliance control has the disadvantage that the apparent stiffness and hence the contact force are dependent on the reaction surface stiffness, but has the advantage of using the same command input (z_r) during both non-contact and contact phases of the task. On the other hand, from experiment 3 it is evident that force control achieves force setpoint tracking regardless of surface stiffness; however requires switching the command input from z_r to F_r during the transition from non-contact to contact tasks. In this section, we present the experimental results for the dual-mode control scheme described in Section 4.3 which combines the advantages of both compliance and force control schemes in a single control] cr.

in this experiment, the end-effector is under dual-mode control with

$$K(s) = 10^{-3} \frac{\alpha s + \beta}{\gamma s + \lambda} \quad (38)$$

The task is to approach the hard surface (steel plate), make an initial contact with a low impact force, and then attain a desired contact force of $F_r = -30Nt$. The force threshold for transition between compliance and force modes is set to $F_T = -3Nt$. For $|F| < 3Nt$, $K(s)$ acts as the compliance controller (33) by setting $\alpha = 0.01$, $\beta = 0.5$, $\gamma = 0.05$, and $\lambda = 1$. For $|F| \geq 3Nt$, the parameters of $K(s)$ are set to $\alpha = 0.05$, $\beta = 1.5$, $\gamma = 1$, $\lambda = 0$ to retrieve the force controller (37). In this experiment, the end-effector is initially commanded to penetrate approximately 5mm inside the contact surface under compliance control, and subsequently servo to the force setpoint of $-30Nt$ under force control after contact has been established. The experimental results are shown in Figure 11a. It is seen that the end-effector impacts the surface gently, and then attains the force setpoint of $-30Nt$, as desired. Thus, the dual-mode controller has the advantages of a small impact force and accurate setpoint tracking. Notice that while in force control, the position command to penetrate into the surface is treated as a disturbance input and is suppressed by the force control] cr.

The experiment is now repeated with the soft surface (cardboard box), and the results are depicted in Figure 11 b. Again, the force response demonstrates a small impact force combined with accurate setpoint tracking. The force response in Figure 11 b has a small overshoot in contrast to Figure 11a due to the low value of the contact surface stiffness.

5.5 Practical Considerations

In the course of the above contact control experiments, we encountered the following practical considerations:

5.5.1 Force Noise

The contact force signal measured by the ATI force/torque sensor contains a significant noise component [12]. This measurement noise has a detrimental effect when the control loop has any differentiating components. To overcome this problem, a first-order filter is often employed and the cutoff frequency is chosen so that the noise frequency lies in the stop-band of the filter. The 'filtered' noise-free force signal is then used in lieu of the 'raw' noisy force measurement. Although filtering of the force signal is an effective means for removing the noise, it inevitably introduces an additional phase-lag into the system which reduces the stability margin and contributes to closed-loop instability. Therefore, a stability analysis must be carried out when the force filter is added to the contact control system.

5.5.2 Effects of α and k_p in Contact Control

The inverse kinematic algorithm that generates the joint setpoints θ_d for the low-level servos requires both the desired Cartesian position X_d and the desired Cartesian velocity \dot{X}_d , see (1). Therefore, the forward path contains a differentiating element acting on X_d to produce \dot{X}_d . The compliance control algorithm consists of the gain k_1 acting on the filtered force and the gain k_2 acting on the raw force. Similarly, the force control algorithm is composed of the gain k_i operating on the raw force integral and the gain k_p operating on the raw force. The integrator in the force control algorithm acts as a low-pass filter and attenuates the effect of the force measurement noise at its output. The proportional gain, on the other hand, passes through the raw noisy force signal and reproduces the noise at its output. Since the raw force signal contains substantial noise, the values of the gain $\alpha (= k_2 \tau)$ in compliance controller and k_p in force control must be very small so that the noisy raw force signal entering the control loop does not drive the system unstable. This fact was confirmed experimentally since in experiments 2 and 3 it was found that increasing α and k_p led to closed-loop instability.

5.5.3 Effect of β in Compliance Control

In the compliance control experiment 2, it was found that β determines the apparent stiffness of the end-effector so that increasing β will lead to a more compliant end-effector; namely $k_{ap} = [k_f^{-1} + \beta]^{-1} = [1 + \beta k_f]^{-1} k_f$. The stability of the closed-loop compliance control system is determined by the loop gain βk_f . Therefore, when the reaction surface is soft, a large value for β can be used yielding a very compliant end-effector; for instance, when the end-effector is held by the human hand which is naturally compliant, it can be made to behave like a soft spring. On the other hand, when contacting a hard reaction surface, a small value of β must be used to ensure stability, and this reduces the end-effector compliance.

5.5.4 Effect of k_i in Force Control

It was found in experiment 3 that k_i determines the speed of response of the contact force to the for-cc setpoint. When k_i is small, the response is sluggish and decreasing k_i will increase the response time. On the other hand, when k_i is large, the contact force responds rapidly with some oscillations, and increasing k_i will result in increased oscillations and ultimately instability. The stability of the closed-loop force control system is governed by the loop gain $k_i k_f$. This implies that in contact with hard surfaces, a small value of k_i must be used; whereas for soft cent acts, a large value of k_i can be adopted.

5.5.5 Effect of Sampling Frequency

In all contact control experiments, it was found that lowering the sampling frequency of the control system necessitates a reduction in the controller gains in order to maintain closed-loop stability. This, in turn, leads to a poor system performance. On the other hand, increasing the sampling frequency allows higher controller gains to be used without encountering instability, which leads to an improved system performance. Therefore, since the contact control algorithms can be evaluated very fast, the sampling frequency was chosen as 400Hz, which is the highest frequency achievable in our experimental system.

6 Contact-Based Eddy-Current Inspection Task

In this section, we describe the utilization of the contact control schemes discussed in Section 4 to perform a contact-based eddy-current inspection task. The purpose of the task is to detect fine cracks on a surface that are not noticeable using vision-based inspection techniques. The eddy-current sensor is a small probe approximately 3 mm in diameter and 2 cm long. The eddy-current sensor is installed on the end-effector close to the tip of the gripper.

To perform the inspection task in the Remote Surface Inspection Laboratory, the manipulator is operated from the graphical user interface which resides on the IRIS Workstation. This interface is expanded to include features for the eddy-current inspection task, such as selecting the control mode for each Cartesian DOF, setting parameter values of the contact controllers, specifying the desired force setpoint and force threshold, displaying the values of the contact forces and torques, and defining the scan path. To perform the task, we use the compliance, force, and dual-mode control schemes described in Section 4. The control is executed at the tool frame $\{T\}$ attached to the tip of the end-effector, which is represented relative to the world frame $\{W\}$ by the six coordinates: p_x, p_y , and p_z positions and ϕ_x, ϕ_y ,

and ϕ_z orientations. The advantage of using the tool frame $\{7'\}$ for eddy-current inspection is that the task can be performed with the inspection surface in *any* orientation in the workspace using the *same* controller parameters. Each of the six end-effector coordinates $\{p_x, p_y, p_z, \phi_x, \phi_y, \phi_z\}$ can be operated independently from the graphical user interface in any of the four control modes: position(I), compliance(C), force(I'), and dual(I). The selectability of control mode for each Cartesian DOF provides the user with considerable flexibility and versatility for executing different phases of the task.

The complete eddy-current inspection task is comprised of six phases: (i) staging, (ii) approach/touching, (iii) leveling, (iv) scanning, (v) relaxing, and (vi) retracting. Each phase is now described briefly:

6.1 Staging Phase

In this phase, the end-effector is operated in the [P,P,P,P,P,P] control mode, i.e. all DOFs are in position mode. Using an autonomous position command, the end-effector is moved to a 'staging' position and orientation facing the inspection surface at a distance of approximately 10cm.

6.2 Approach/Touching Phase

The end-effector control mode is now set to [F,F,D,F,F,F], with the force and torque setpoints in I'-mode specified as zeros and the force threshold level in D-mode set as $F_T = 3Nt$. The end-effector is now commanded to move forward and touch the surface. Since the end-effector translational z motion is now under compliance control, the forces sensed by the wrist-mounted sensor are used to reduce the apparent stiffness of the end-effector, thereby reducing the impact forces at contact. This results in a gentle contact between the end-effector and the surface.

6.3 Leveling Phase

Since the end-effector can potentially contact the surface at a tilted configuration, it is necessary to level the end-effector on the surface before initiating the scanning motion. This is accomplished by using the previously-set control mode [F,F,D,F,F,F]. This causes changes in the end-effector position and orientation to nullify the forces and torques generated due to an unlevel contact. The force control algorithm reduces the unwanted forces and torques to

zero and makes the gripper fingers pivot and level themselves. At the end of this phase, both fingers are in full contact with the inspection surface.

6.4 Scanning Phase

In this phase, the end-effector is operated in the [P,P,D,F,F,F] control mode. The P-modes in the translational x and y axes cause the motion of the end-effector on the surface. The D-mode in the translational z axis maintains a constant contact force of $F_z = 20N$ during scan. The F-mode with $T_z = 0Nm$ ensures a good level contact between the end-effector and the surface during the entire scan. The scan path is typically a back-and-forth motion, and the scan lines are approximately 20 cm long and separated by 2 cm. The user designates the scan path from the IRIS to cover the square ABCD of interest on the inspection surface. The path begins at the user-designated start point A and performs a raster scan to reach the end point D. The user can specify the length and separation of the scan lines, and time for completion. The scan path is given to the manipulator control system in the form of a sequence of via-points for trajectory generation,

6.5 Relaxing Phase

After the completion of the inspection, the force exerted by the end-effector on the surface is relaxed prior to retraction. This is achieved by operating in the [P,P,D,F,F,F] control mode with a small force setpoint of $F_z = 4N$, so that the end-effector is barely touching the surface.

6.6 Retracting Phase

In this phase, the end-effector is operated in the [I,I,I,I,I,I] control mode. In this case, position commands are issued to move the end-effector to a pre-defined position and orientation so that it faces the surface at a distance of approximately 10cm. This completes the eddy-current inspection task from the arm control perspective.

Figures 12a-12c and 13a-13c depict the variations of the forces and torques in the tool frame exerted by the end-effector during the entire inspection task. It is seen that the torques are reduced to zero by the controller to ensure leveling, while the contact force is maintained around the desired setpoint throughout the scanning operation.

7 Conclusions

Three control schemes for manipulators in contact with their environment are described in this paper. The control schemes are pragmatic since they are based on the existing position control system provided by the robot manufacturer. This makes the schemes easily implementable on industrial manipulators where access to the joint torques is often not provided.

Another important feature of the proposed control schemes is their simplicity which leads to very fast computational algorithms. This enables the use of a high sampling frequency in the digital control implementation of the control schemes. The frequency of sampling is a critical issue in contact control schemes, since the control loop contains a typically large gain associated with the environmental stiffness which makes the closed-loop system unstable at low sampling frequencies. In addition to enhanced stability, a high sampling frequency allows larger gains to be used in the contact controller which, in turn, lead to improved system performance.

Finally, it is noted that the dual-mode contact controller presented in this paper is constructed from the compliance and force control modes to soften the initial impact with the surface and subsequently achieve force regulation. This combines the attractive features of both the compliance and force control schemes into a unified single gain-scheduling contact controller which enjoys the advantages of compliance and force control, without suffering from their shortcomings. This is accomplished by operating as a compliance controller at initial impact with the reaction surface to reduce the force imparted on the surface, and then switching automatically to force control to regulate the contact force when the initial contact has been established. In this manner, each control mode is utilized when it is most appropriate. Thus the dual-mode controller provides a practical solution to the impact control problem.

8 Acknowledgments

The research described in this paper was carried out at the Jet Propulsion Laboratory, California Institute of Technology, under contract with the National Aeronautics and Space Administration. Fruitful technical discussions with J. Balaram, S. Hayati, and G. Tharp on the inspection task in Section 6 are gratefully acknowledged.

9 References

- [1] N. hogan: "Impedance control: An approach to manipulation, Parts 1-111", ASME Journal of Dynamic Systems, Measurement, and Control, Vol. 107, No. 1, pp. 1-24, 1985.
- [2] H. Kazerooni, T.B. Sheridan, and P.K. Houpt: "Robust compliant motion for manipulators, Parts I-II", IEEE Journal of Robotics and Automation, Vol. RA-2, No. 2, pp. 83-105, 1986.
- [3] M. Raibert and J. Craig: "Hybrid position/force control of manipulators", ASME Journal of Dynamic Systems, Measurement, and Control, Vol. 102, No. 2, pp. 126-133, 1981.
- [4] S. Hayati, J. Balaram, H. Seraji, W.S. Kim, and K.S. Tso: "Remote surface inspection system", Robotics and Autonomous Systems, Vol. 11, No. 1, pp. 45-49, 1993.
- [5] H. Seraji: "Configuration control of redundant manipulators: Theory and implementation", IEEE Transactions on Robotics and Automation, Vol. 5, No. 4, pp. 472-490, 1989.
- [6] H. Seraji and R. Colbaugh: "Improved configuration control for redundant robots", Journal of Robotic Systems, Vol. 7, No. 6, pp. 897-928, 1990.
- [7] H. Seraji: "Task-based configuration control of redundant robots", Journal of Robotic Systems, Vol. 9, No. 3, pp. 411-451, 1992.
- [8] H. Seraji, M. Long, and T. Lee: "Motion control of 7-DOF arms: The configuration control approach", IEEE Transactions on Robotics and Automation, Vol. 9, No. 2, pp. 125-139, 1993.
- [9] J. Craig: "Robotics: Mechanics and Control", Addison Wesley Publishing Company, New York, Second Edition, 1989.
- [10] K. Kreutz, M. Long, and H. Seraji: "Kinematic analysis of 7-DOF manipulators", International Journal of Robotics Research, Vol. 11, No. 5, pp. 469-481, 1992.
- [11] R. Volpe: "Task space velocity blending for real-time trajectory generation", Proceedings of IEEE International Conference on Robotics and Automation, Vol. 2, pp. 680-687, Atlanta, May 1993.
- [12] R. Volpe and P. Khosla: "Computational considerations in the implementation of force control strategies", Journal of Intelligent and Robotic Systems: Theory and Applications, 1994 (to appear).

[13] H. Seraji: "Adaptive admittance control: An approach to explicit force control in compliant motion", Proceedings of IEEE International Conference on Robotics and Automation, Vol. 4, pp. 2705-2712, San Diego, May 1994.

FIGURE 1: HARDWARE ARCHITECTURE

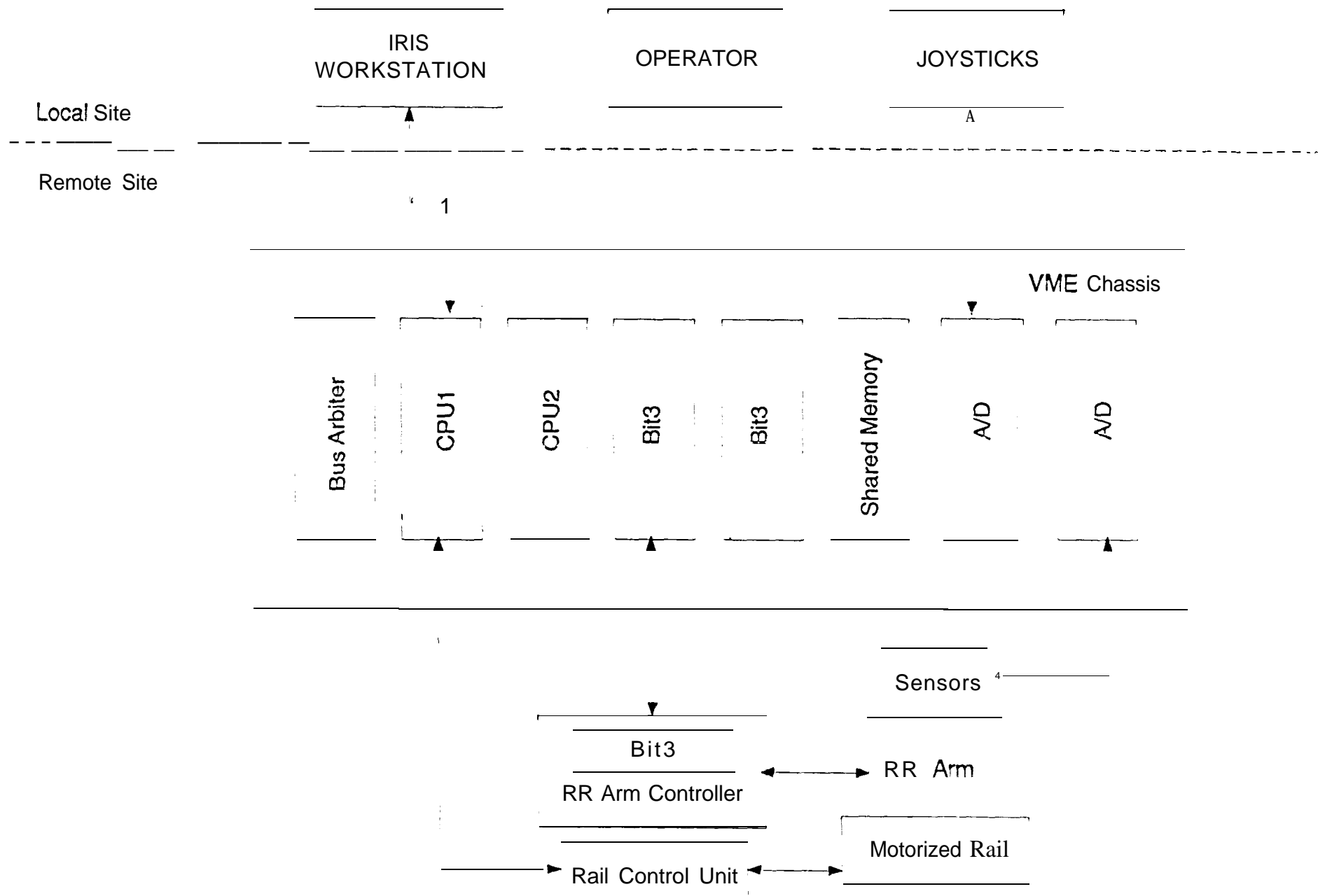
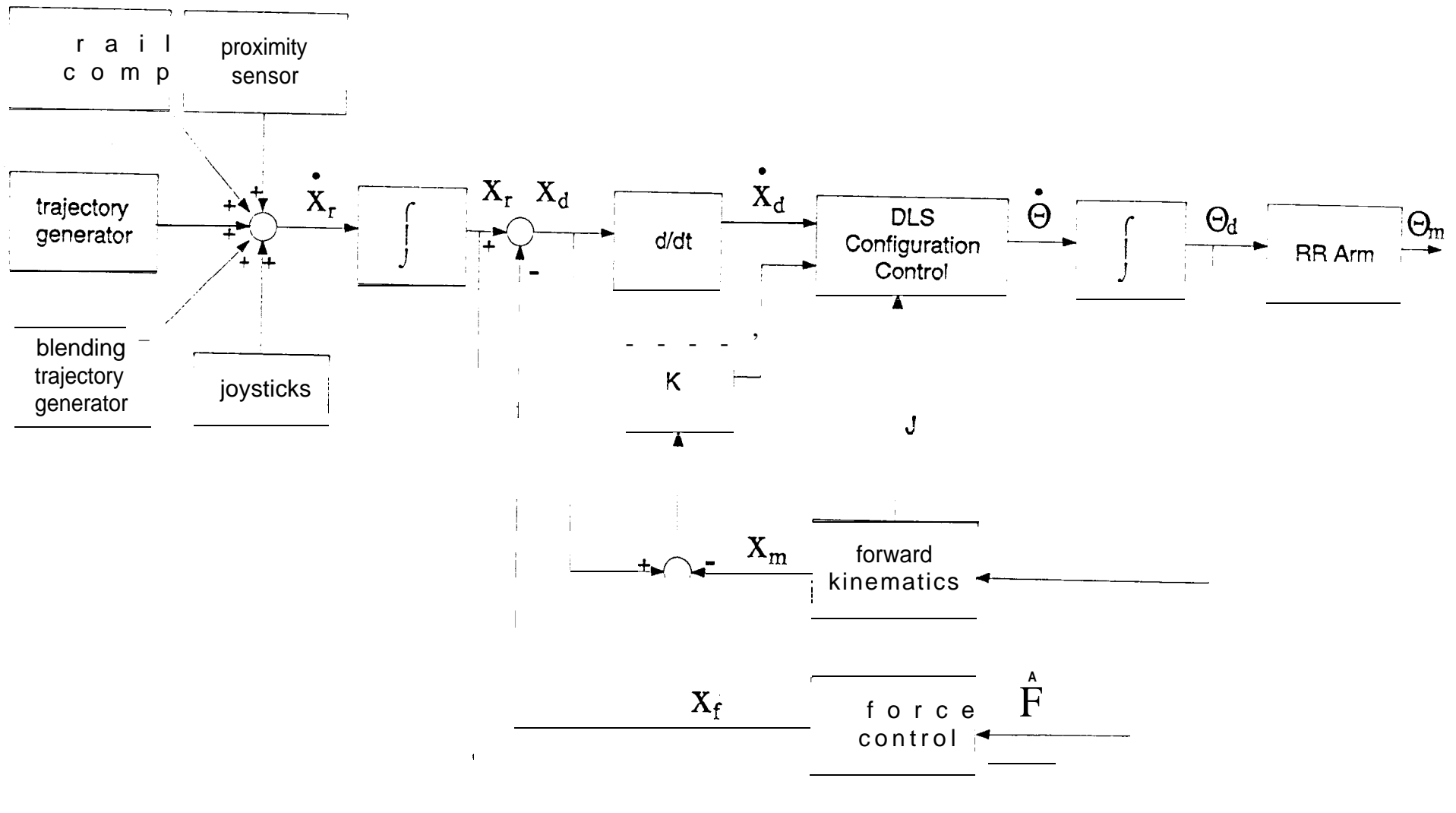


Figure 2: Control Diagram



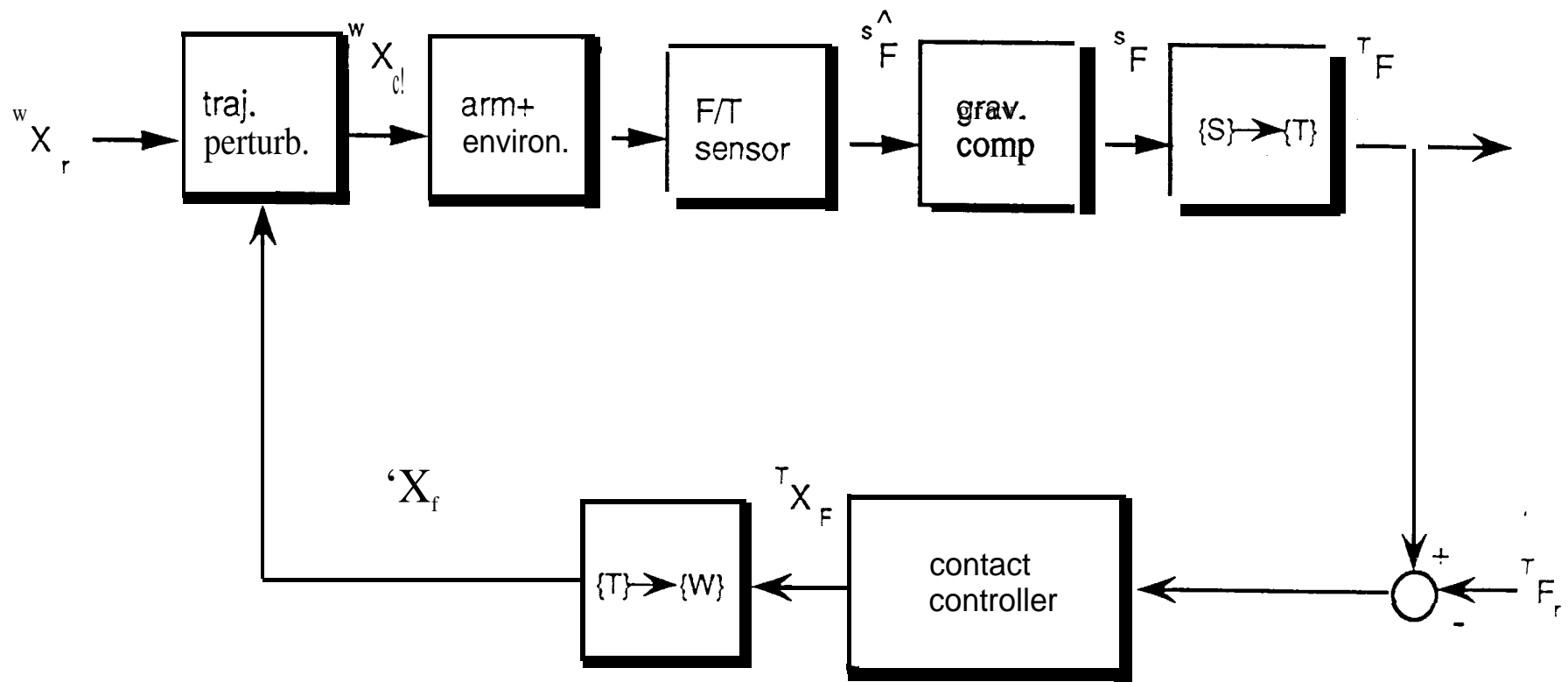
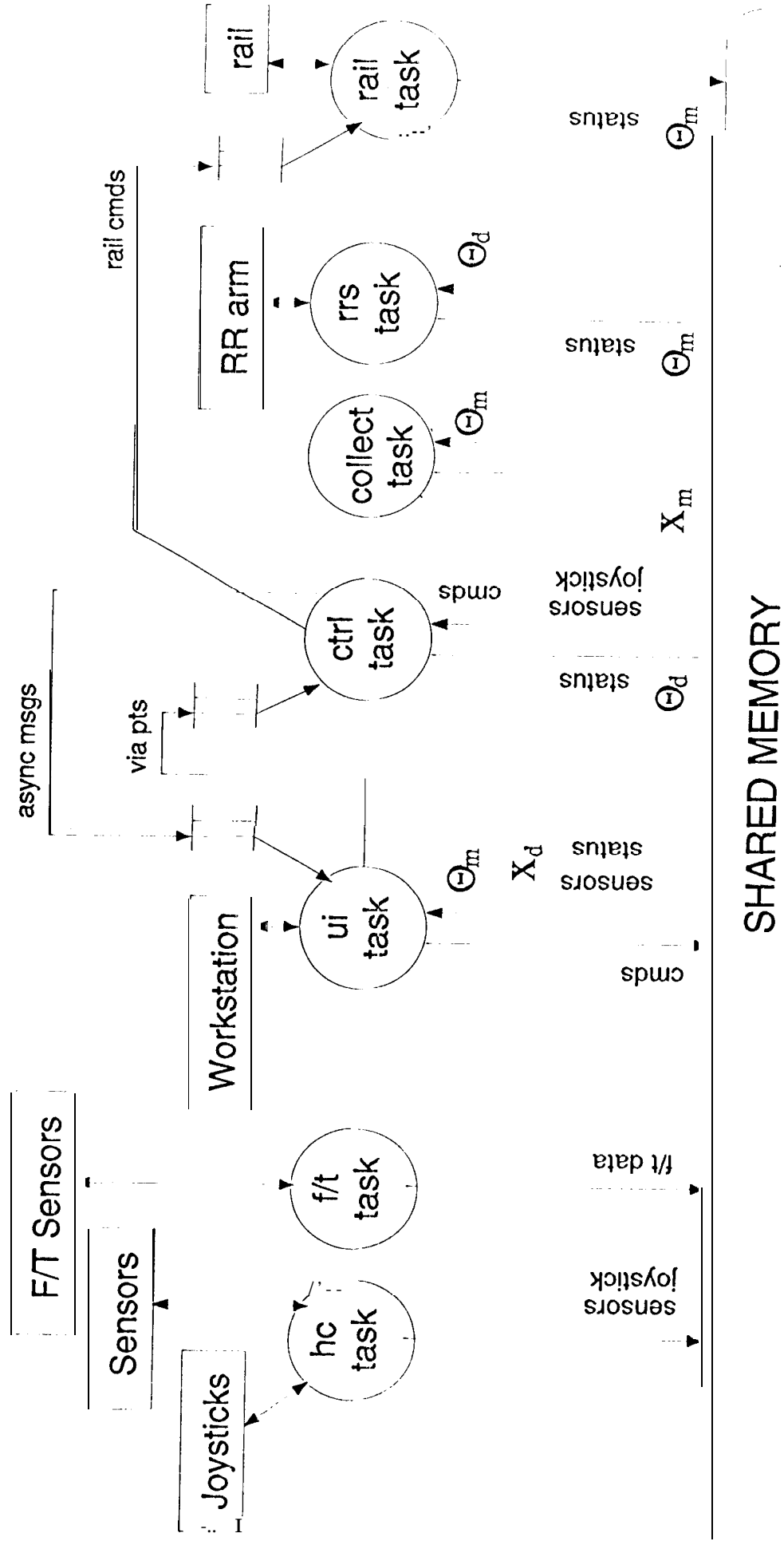


Figure 3: Block Diagram of Contact Control Scheme

Figure 4: Software Architecture



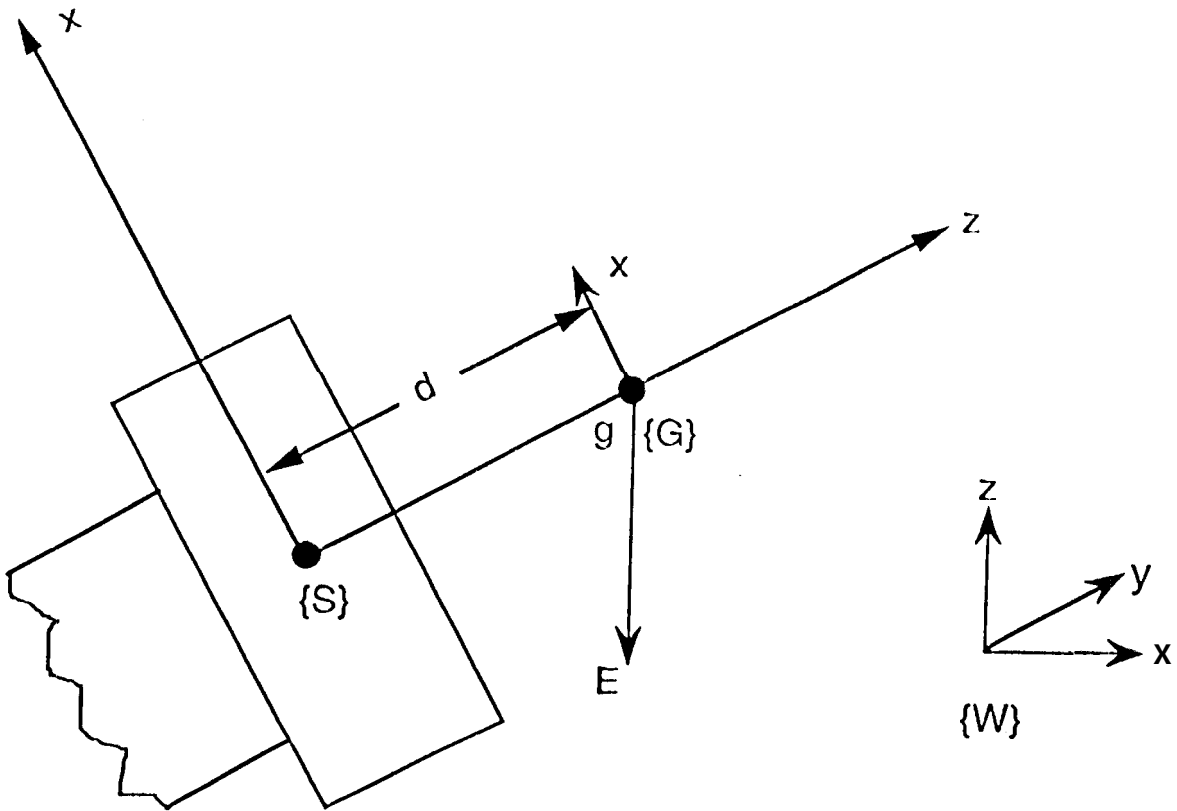


Figure 5. Frame Definition for Gravity Compensation

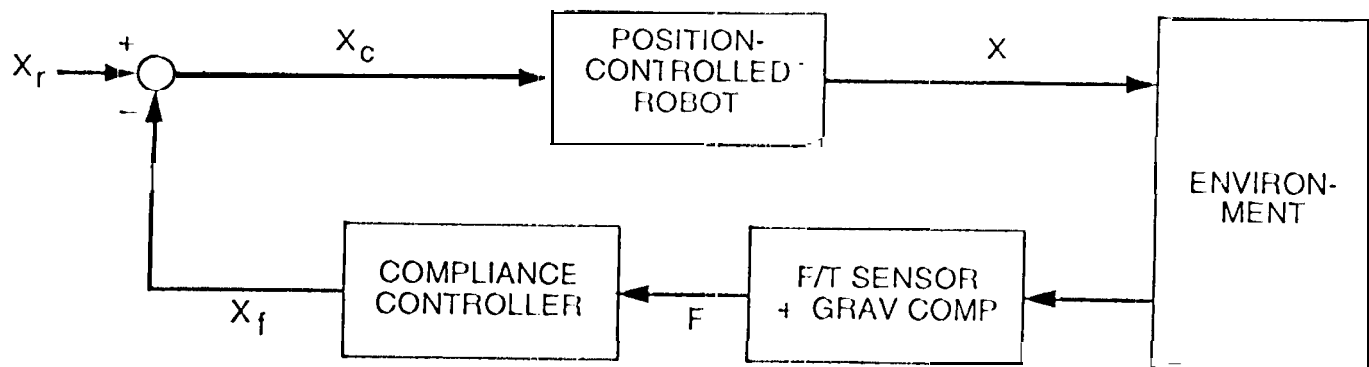


Figure 6. Compliance Control System

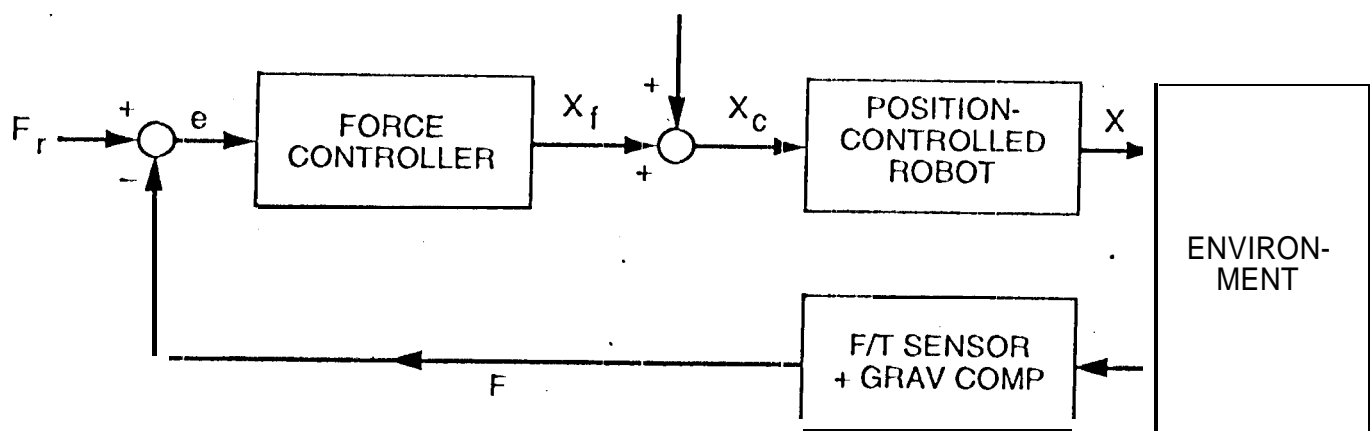


Figure 7. Force Control System

Figure 8a. No Force Control (Hard Surface)

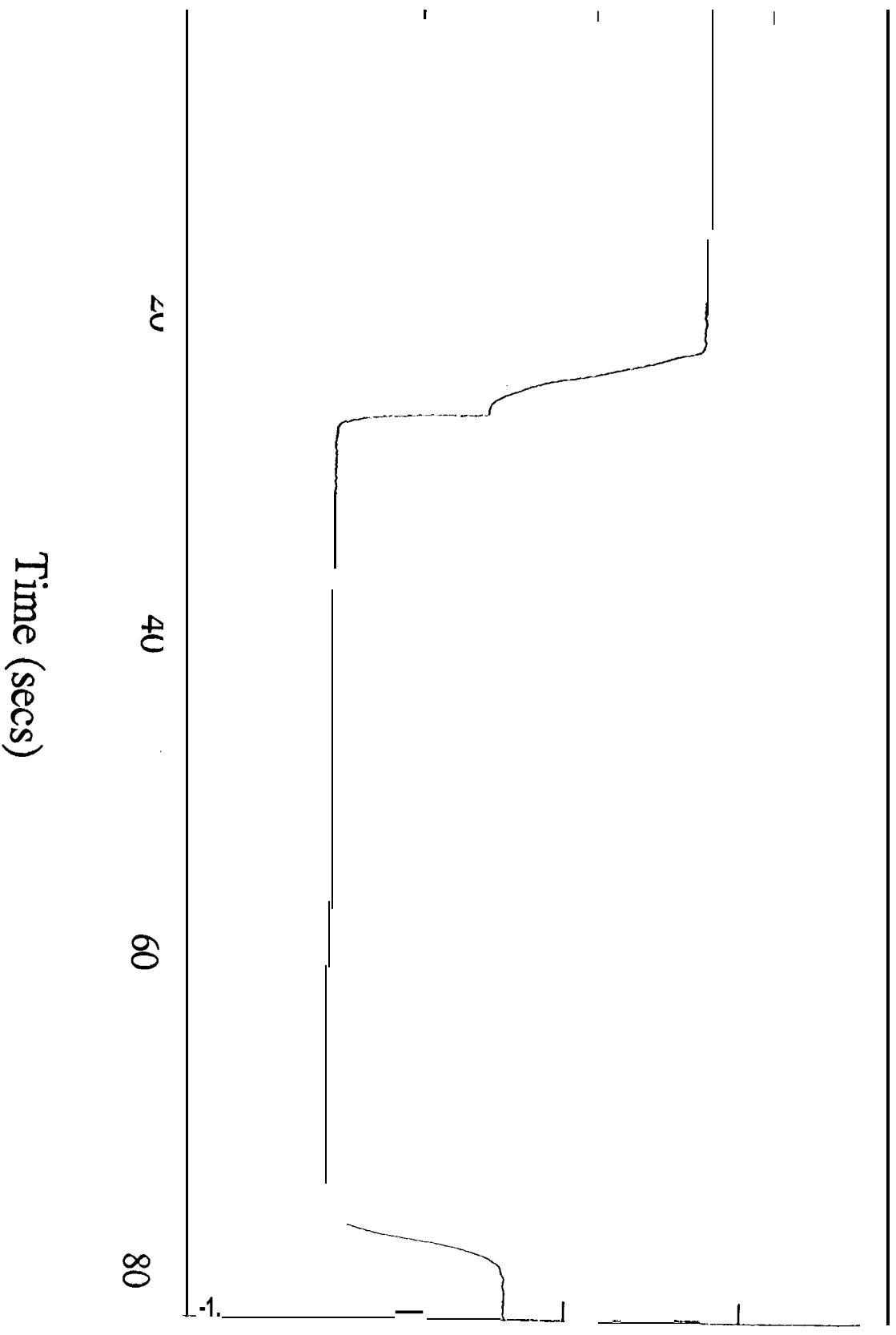


Figure 8b. No Force Control (Hard Surface)

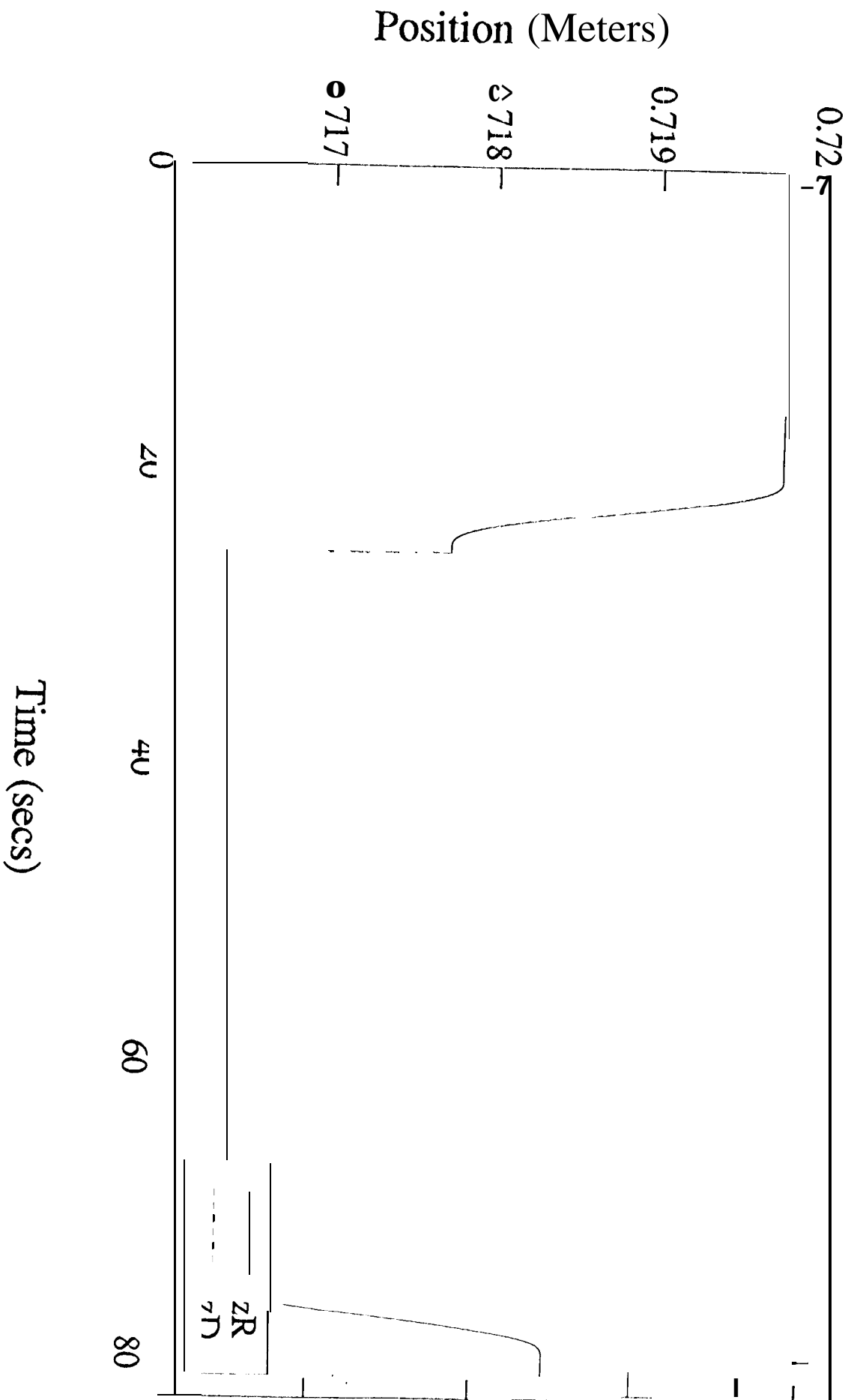


Figure 9a. Compliance Control (Hard Surface)

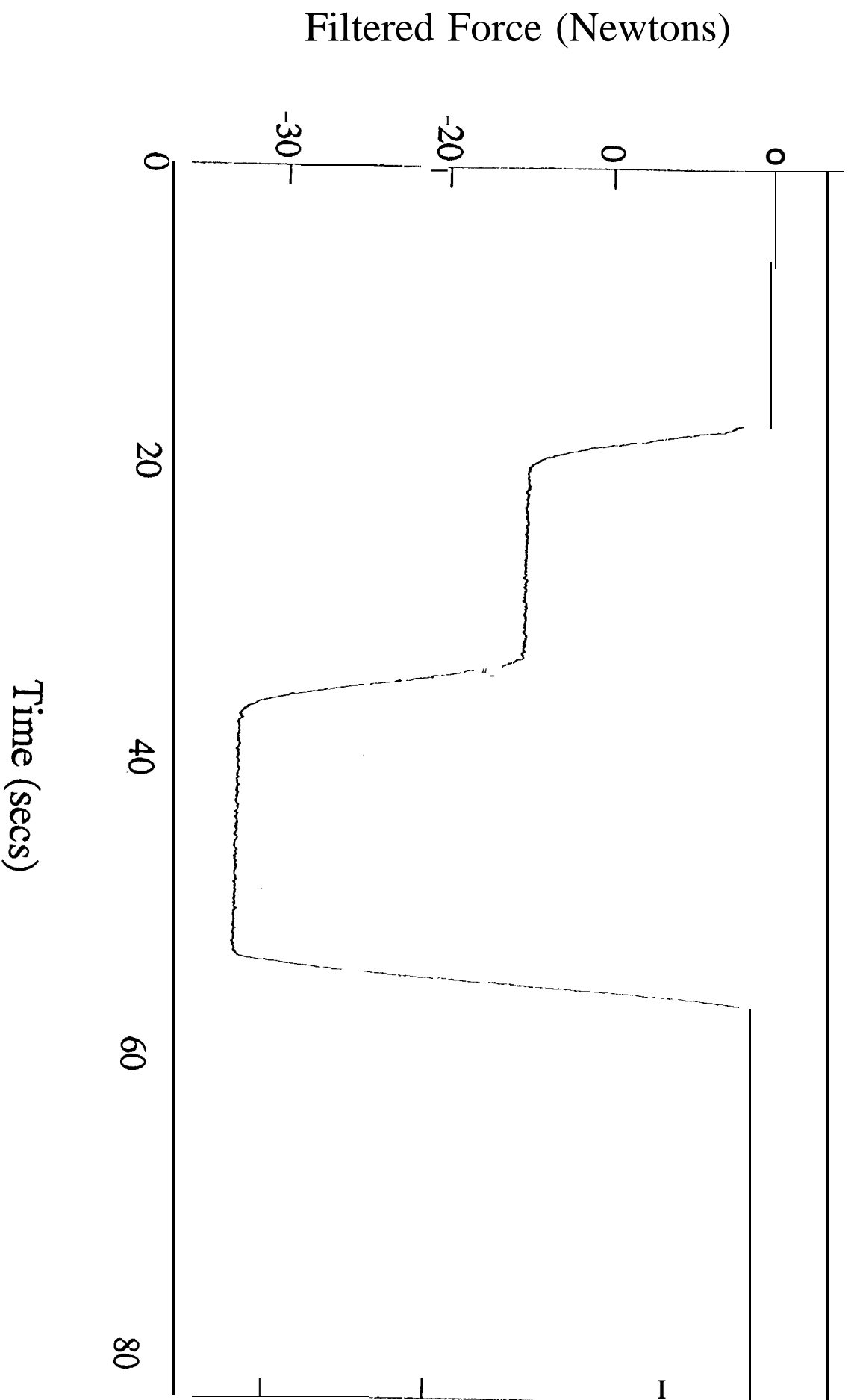


Figure 9b. Compliance Control (Hard Surface)

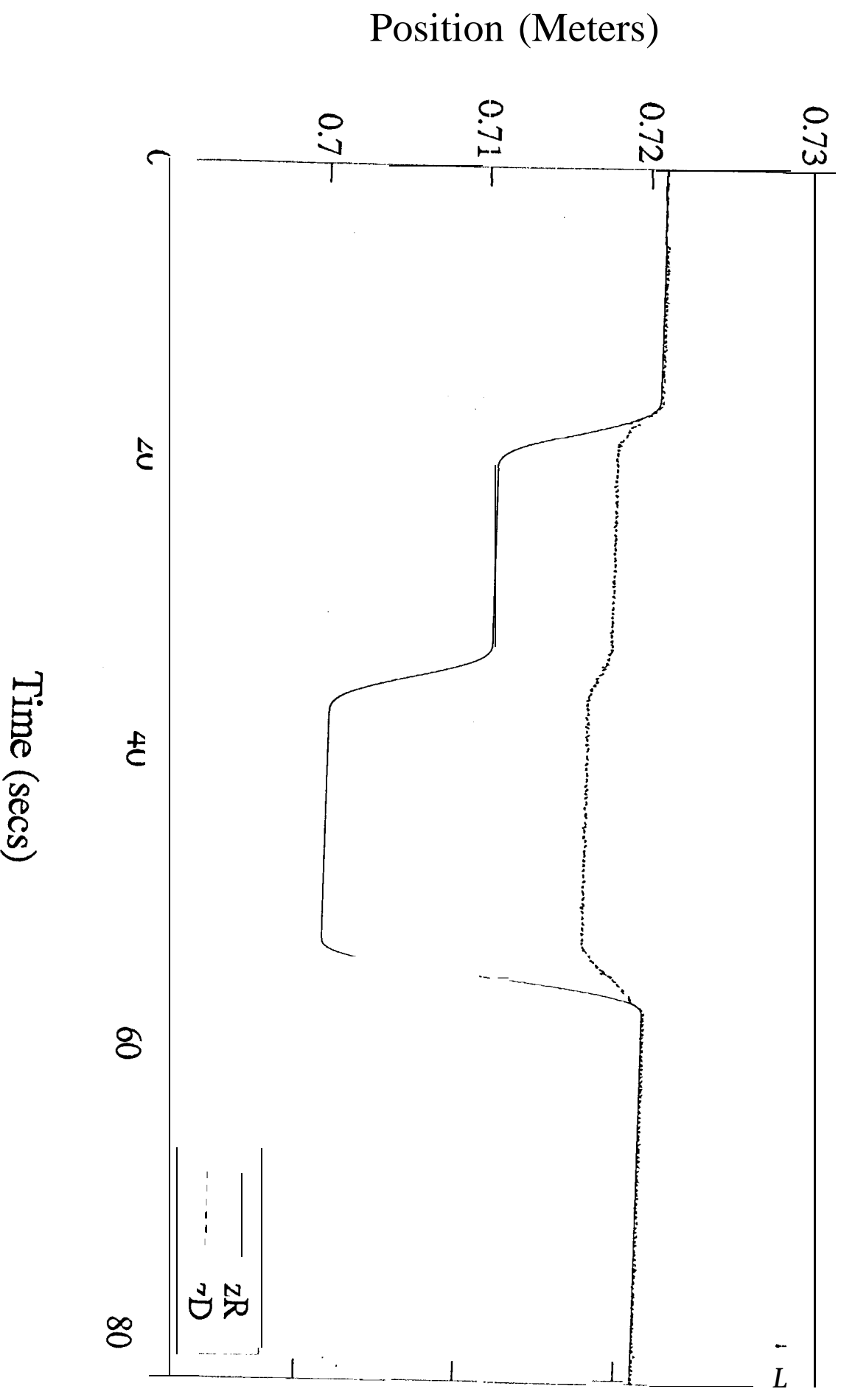


Figure 9c. Compliance Control (Soft Surface)

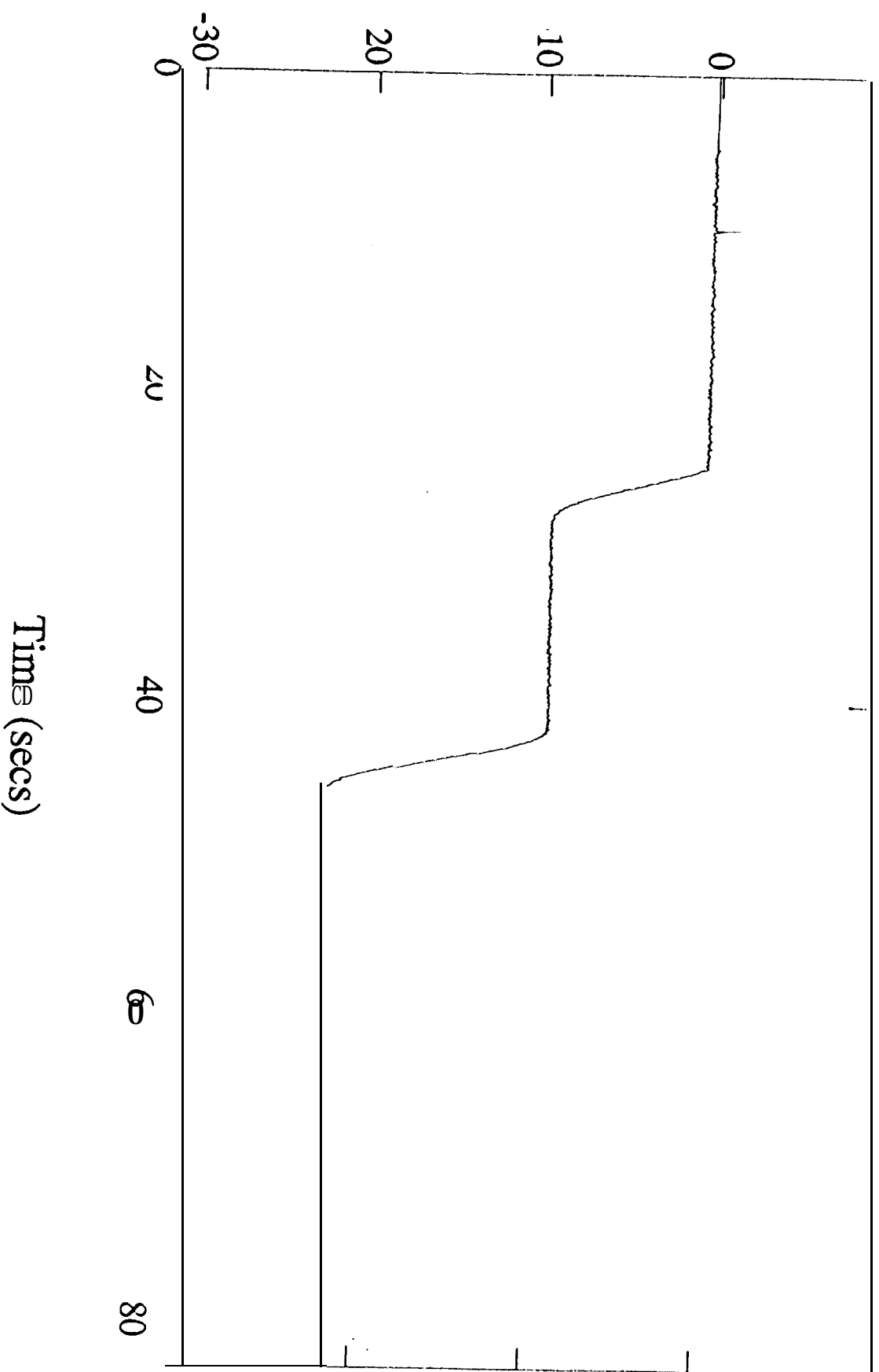


Figure 9d. Compliance Control (Soft Surface)

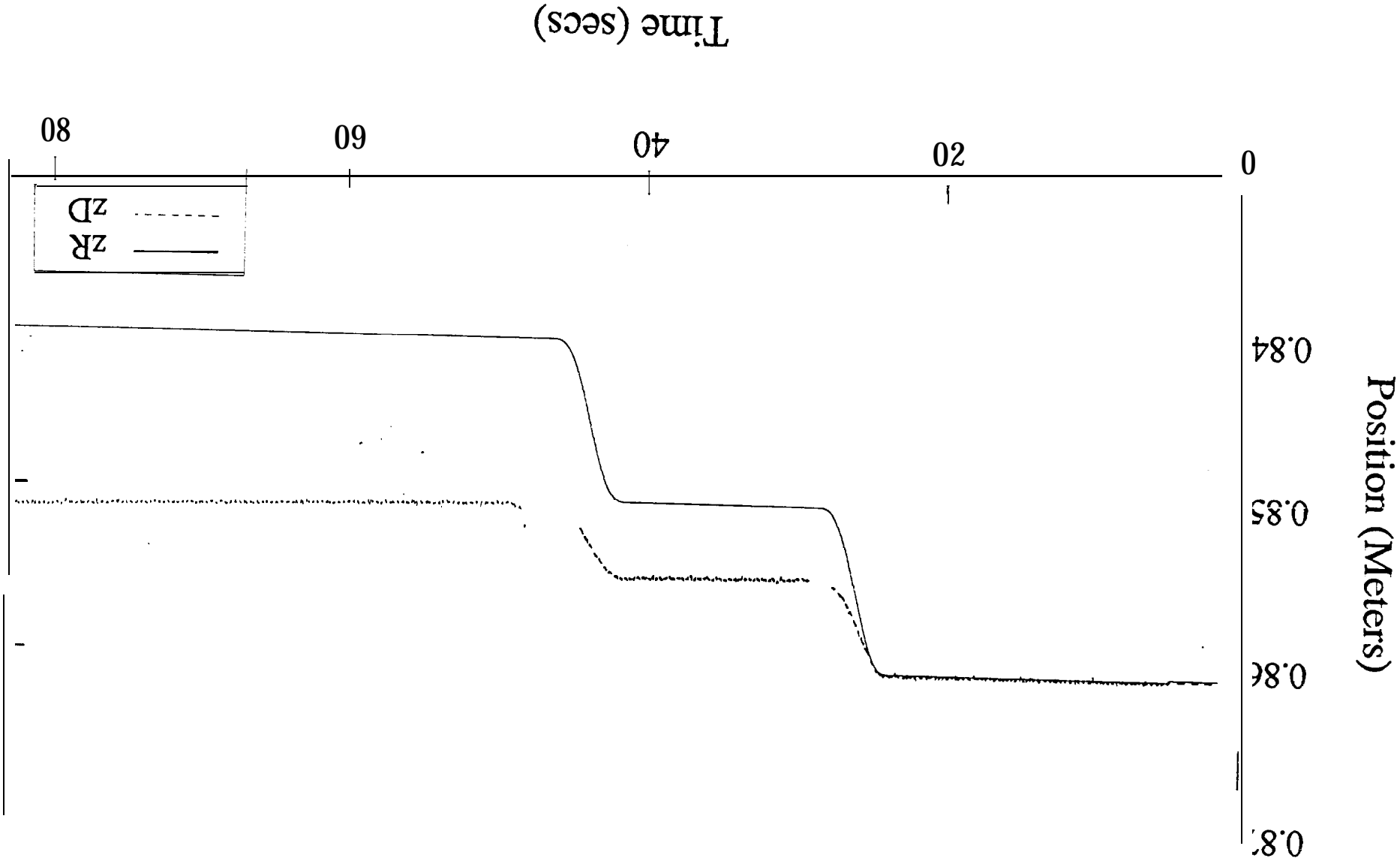


Figure 10a. Force Control (Hard Surface)

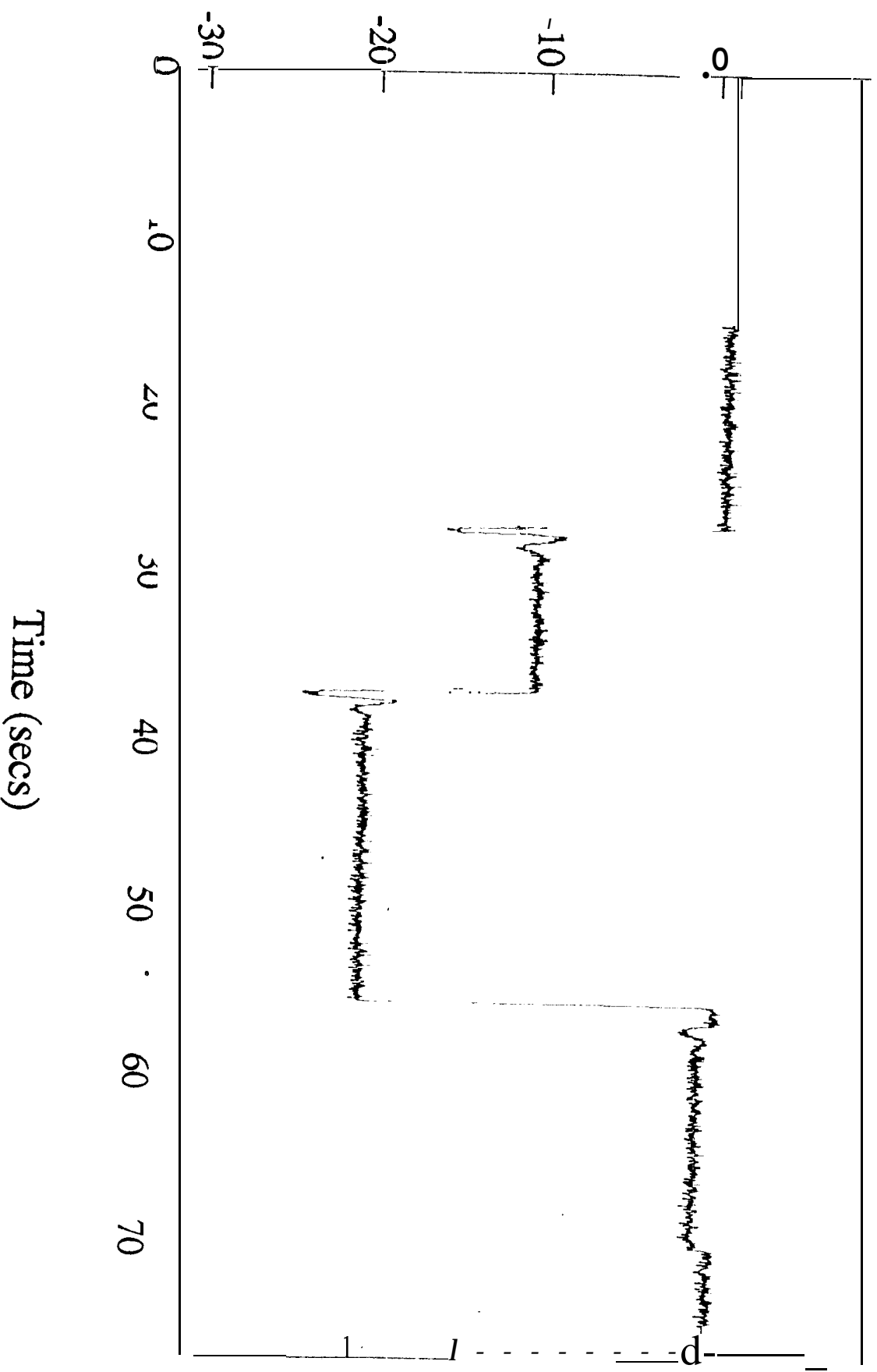


Figure 10b. Force Control (Disturbance Rejection)

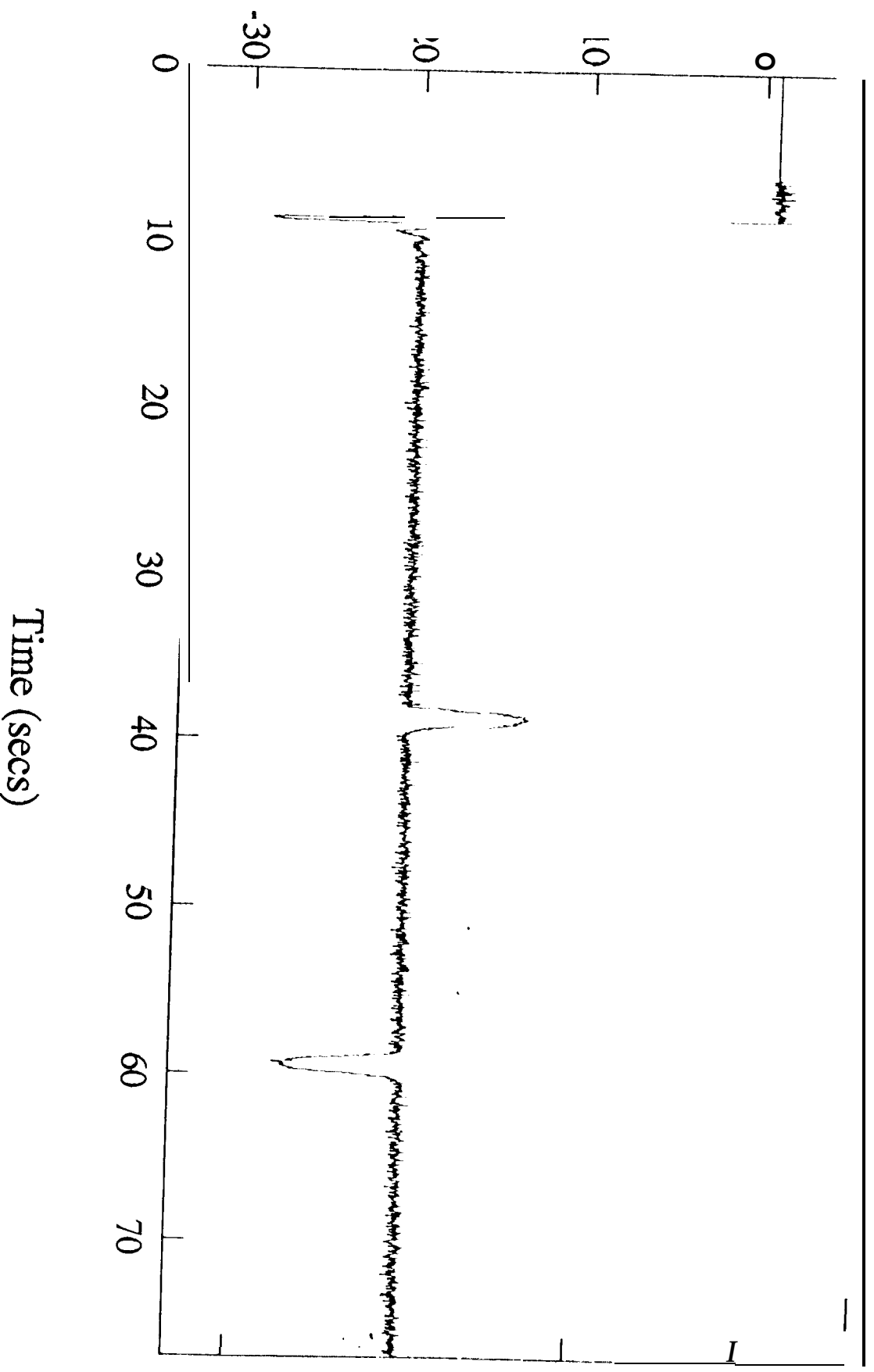


Figure 10c. Force Control (Soft Surface)

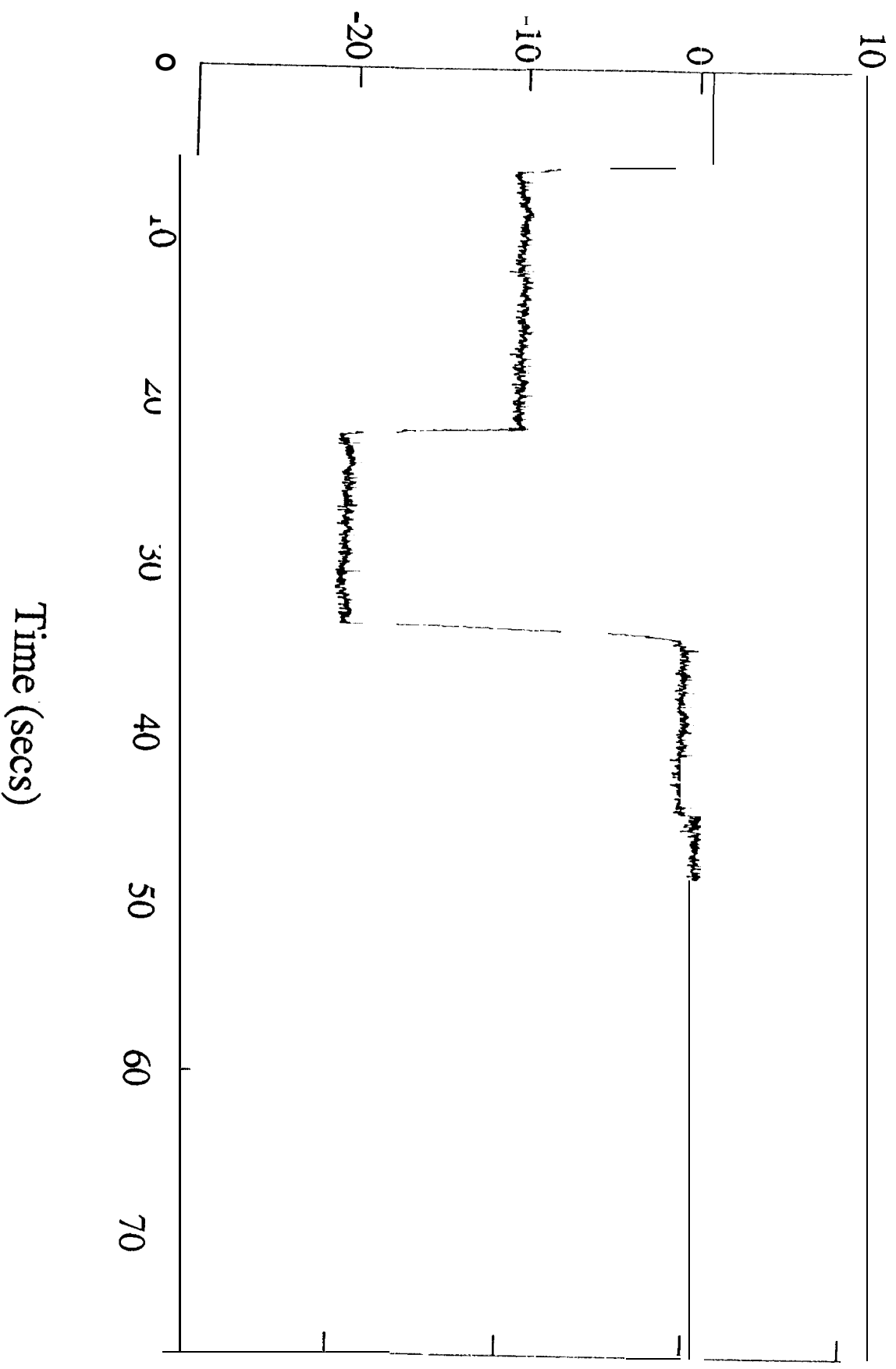


Figure 11a. Dual Mode Control on Hard Surface

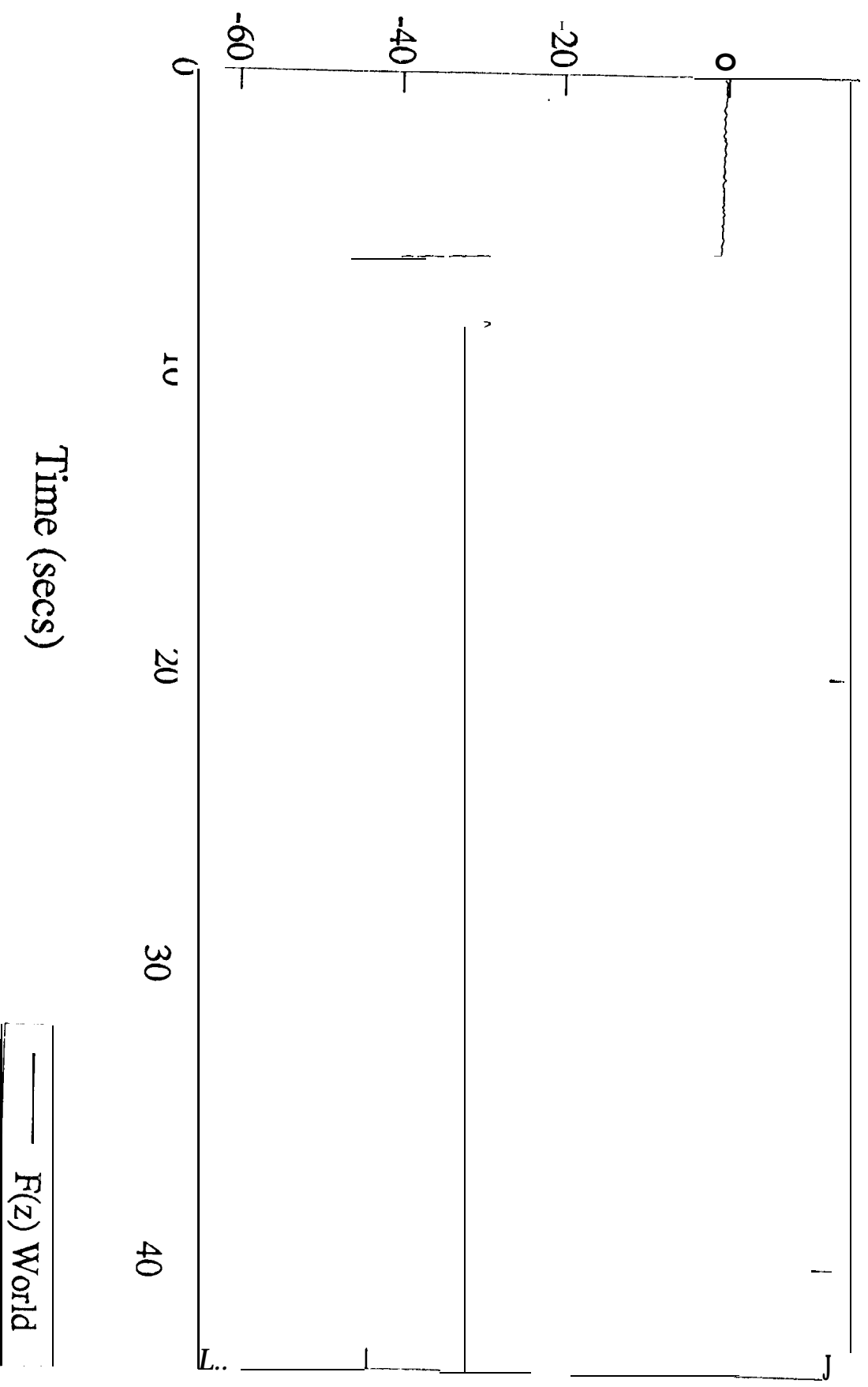


Figure 11b. Dual Mode Control on Soft Surface

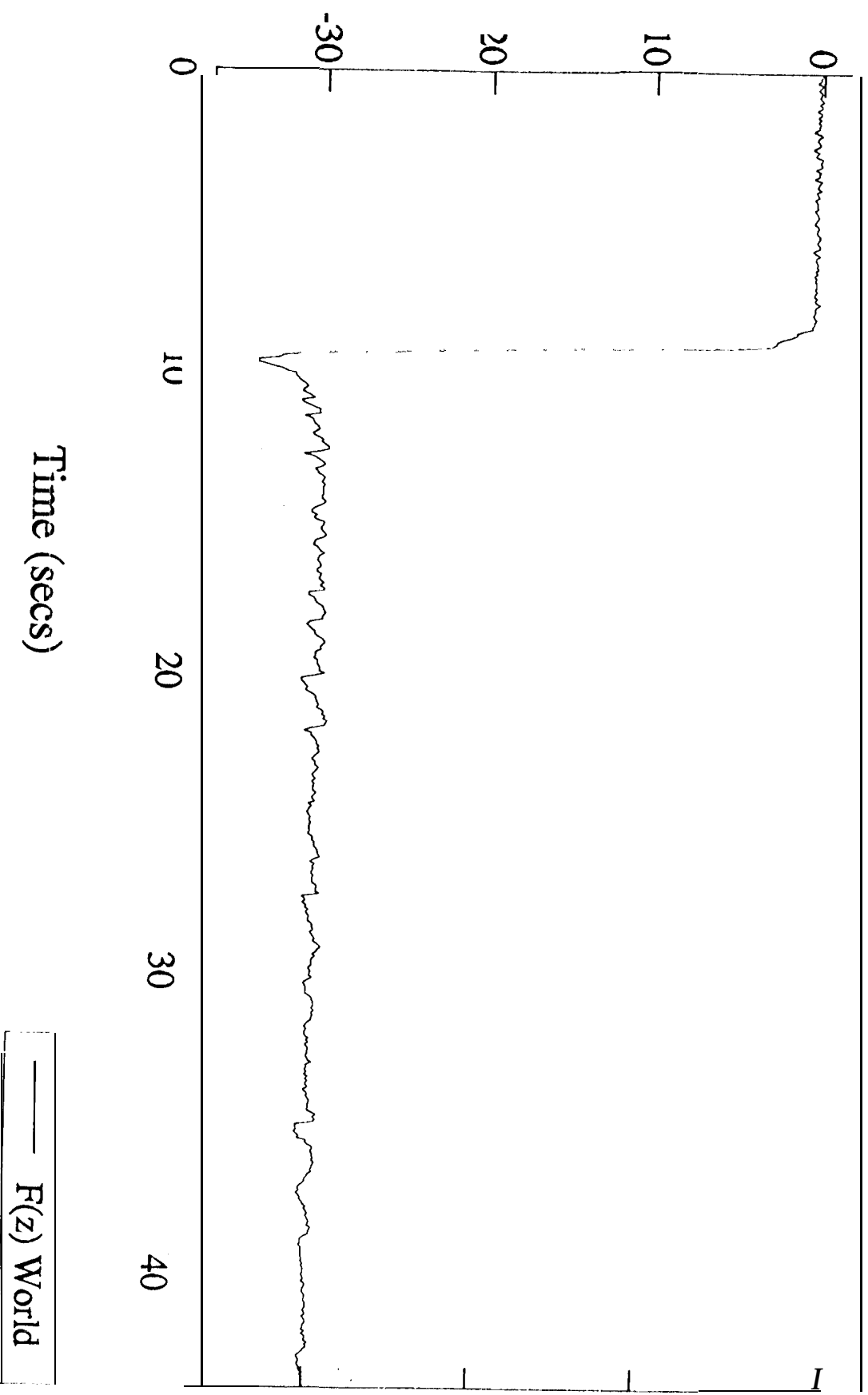


Figure 12a. Forces During Touch and Level Phases

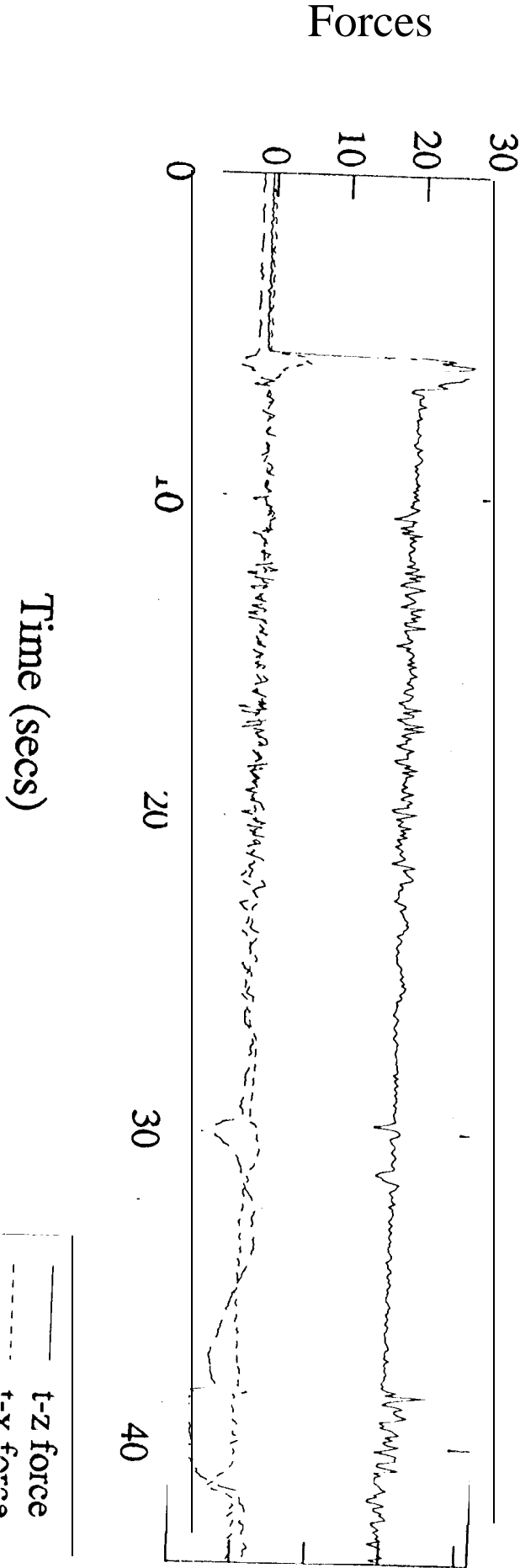


Figure 12b. Forces During Scan Phase

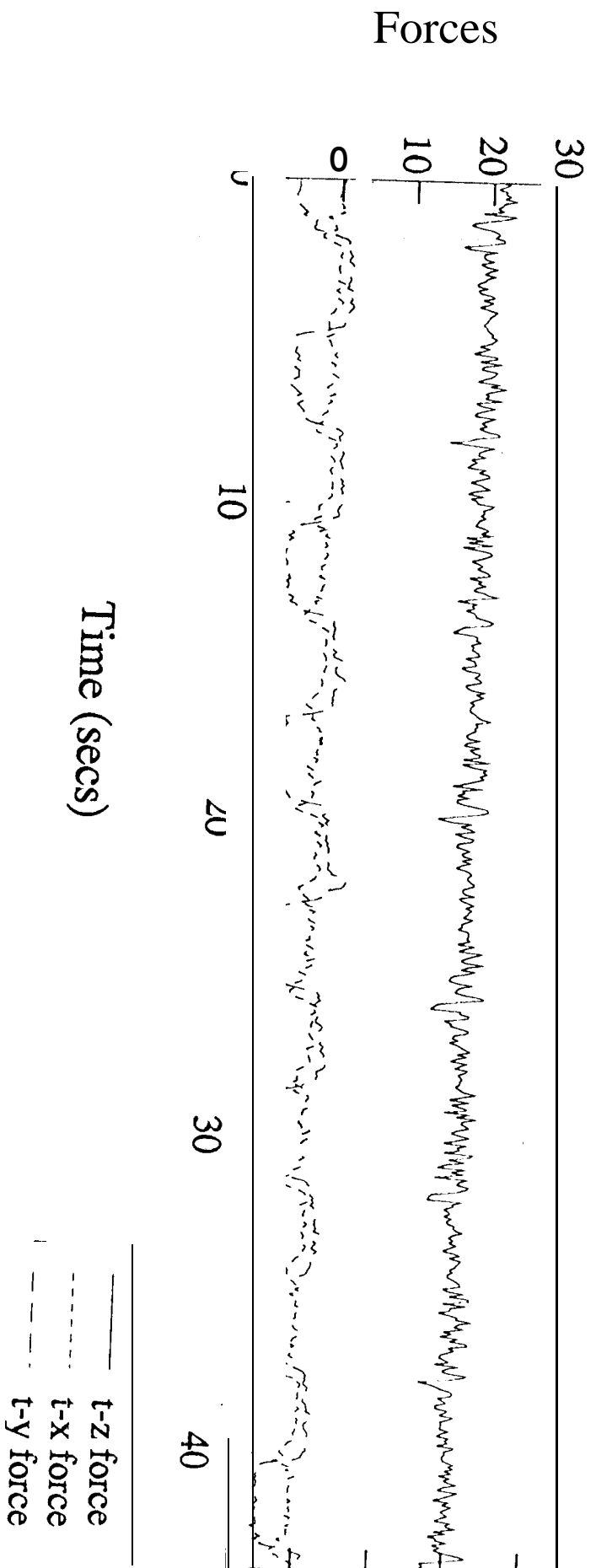


Figure 13a. Torques During Touch and Level Phases

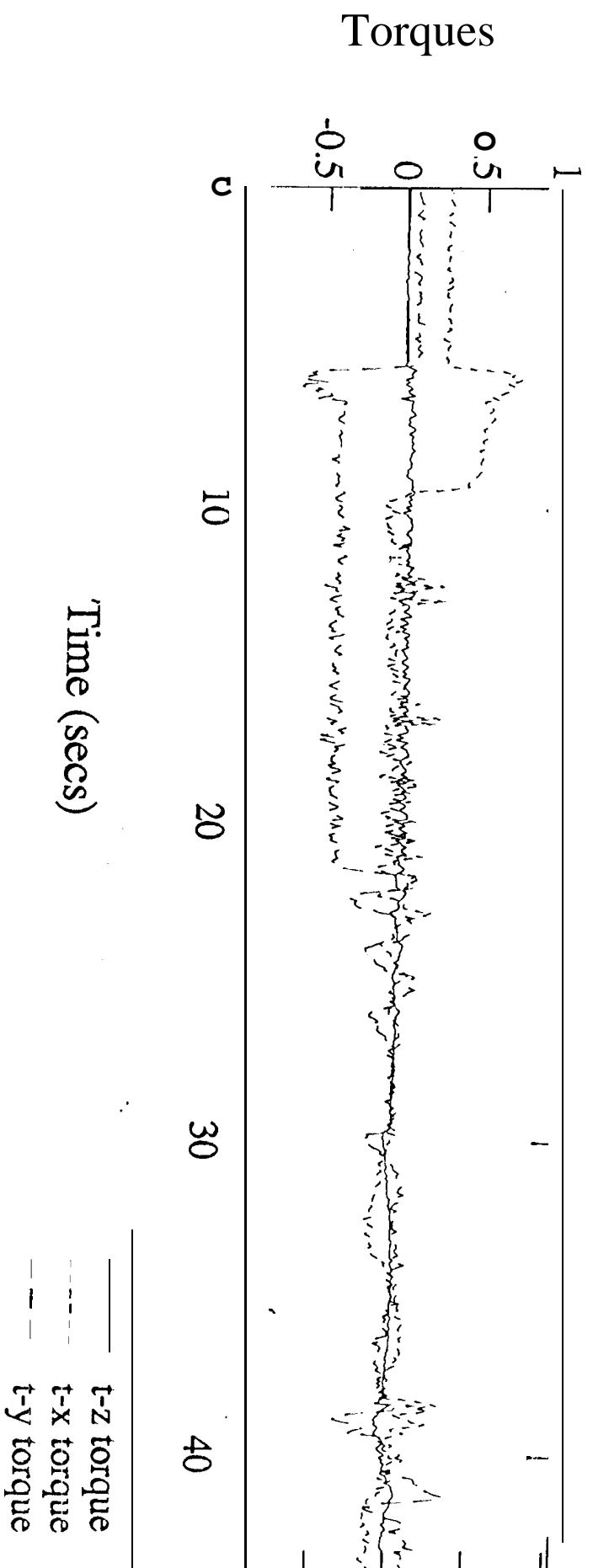


Figure 13b. Torques During Scan Phase

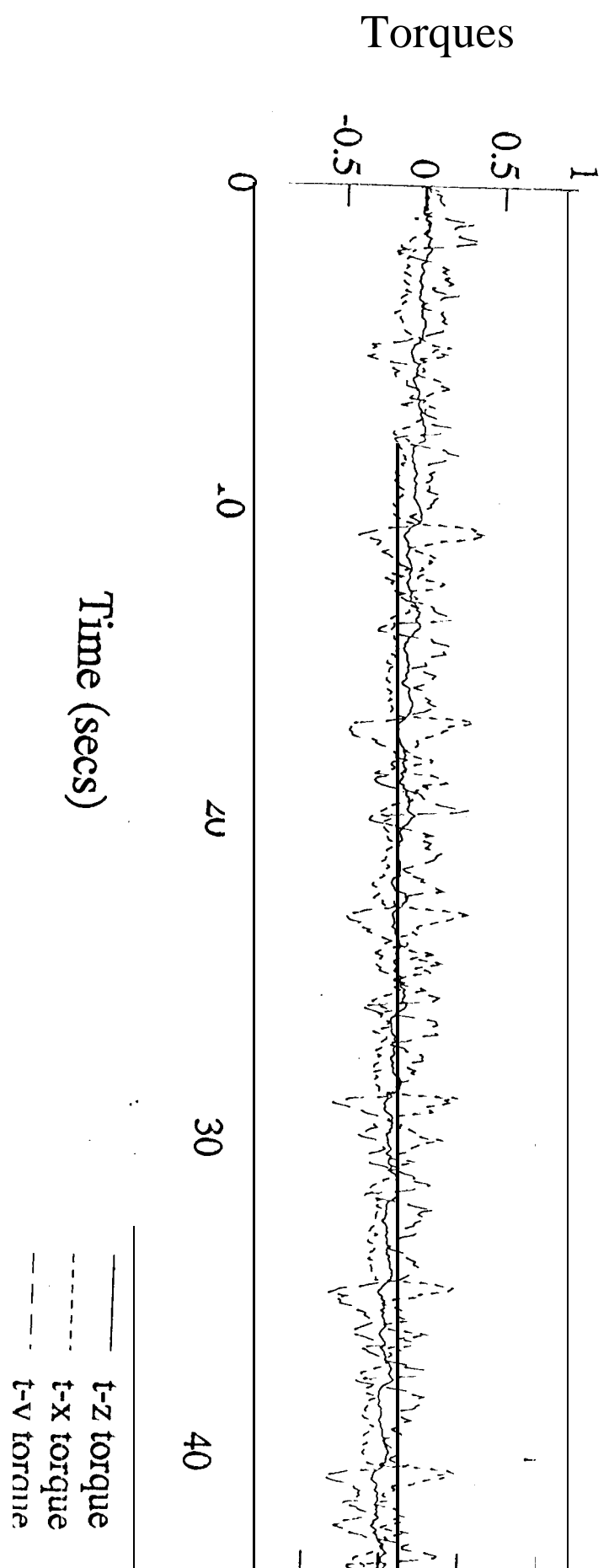


Figure 13c. Torques During Relax and Retract Phases

